Journal of Catalysis 421 (2023) 403–418

Contents lists available at ScienceDirect

Journal of Catalysis

journal homepage: www.elsevier.com/locate/jcat

Role of phosphorous in transition metal phosphides for selective hydrogenolysis of hindered C–O bonds

Conor Waldt [a], Hansel Montalvo-Castro [a], Abdulrahman Almithn [a,b], Álvaro Loaiza-Orduz [c], Craig Plaisance [c], David Hibbitts [a,*]

[a] Department of Chemical Engineering, University of Florida, Gainesville, FL 32608, USA
[b] Department of Chemical Engineering, King Faisal University, Al Hofuf, Eastern Province 31982, Saudi Arabia
[c] Cain Department of Chemical Engineering, Louisiana State University, Baton Rouge, LA 70803, USA

ARTICLE INFO

Article history:
Received 29 November 2022
Revised 3 February 2023
Accepted 19 February 2023
Available online 23 February 2023

Keywords:
DFT
Catalysis
Transition metal phosphides
C–O hydrogenolysis

ABSTRACT

C–O hydrogenolysis can upgrade biomass to higher value chemicals, but often requires the selective activation of sterically hindered C–O bonds. Previous work examining C–O hydrogenolysis of methyltetrahydrofuran (MTHF), a model biomass-derived molecule, has shown that Ni_2P and $Ni_{12}P_5$ show higher selectivities toward activation of the hindered (^{3}C–O) bond over the unhindered (^{2}C–O) bond compared to pure Ni catalysts. These measured selectivity differences—favoring ^{3}C–O activations for materials with higher P content—were consistent with calculated free energy barriers for the ^{2}C–O and ^{3}C–O activation pathways using density functional theory (DFT). However, the role of P in causing this shift in selectivity is still unknown. In this work we use DFT to study other transition metal phosphides (Co_2P, Pd_2P, Rh_2P, Fe_2P, and Ru_2P) and contrast them to their pure metal counterparts to determine if the role of P in Ni_2P materials is consistent across other transition metals. To do this, we constructed theoretical models of these other transition metal phosphides that were isostructural to the $Ni_2P(001)$ surface. In comparing the phosphide materials to their pure metal counterparts, we saw a nearly ubiquitous shift in selectivity towards hindered C–O activation. However, the magnitudes of these shifts were significantly varied, with only Ni_2P and Pd_2P predicted to show high selectivity toward ^{3}C–O activation. Periodic trends and charge analysis suggest that the varied selectivity shifts (comparing metal-phosphide to pure metal) can be rationalized based on the electronegativity of the metal and the resultant charge-transfer between P and the nearby metal atoms, which typically results in metals with a positive partial charge showing greater ^{3}C–O selectivity. These results help to deconvolute the electronic and geometric impacts of P incorporation into transition metal catalysts and identify new catalysts for selective C–O activation at hindered C-atoms.

1. Introduction

An abundance of unused biomass materials are available for the production of biofuels and other commodity chemicals, the latter being mainly produced from non-renewable fossil deposits.[1–3] Many forms of biomass are difficult to process via conventional microbial decomposition because of their high lignin content.[4] Pyrolysis is used to depolymerize the lignin to access the more enzymatically digestible biomass material—typically polysaccharides. This material, in turn, is deconstructed into mixtures of smaller oxygenates (e.g., alcohols, ketones, furans, pyrans, and aromatics), also called bio-oil.[1,4–7] The conversion of these oxygenates into high-value chemicals (e.g., α,ω-diols)[5,8–10] requires the rupture of C–O bonds, whose selective cleavage is desired to minimize hydrogen consumption. The selective rupture of specific C–O bonds with competing C–C bond cleavage, however, is still a major challenge.[5,8,11]

A model compound for studying the selective C–O hydrogenolysis in biomass derived oxygenates is 2-methyltetrahydrofuran (MTHF), because it contains two chemically distinct C–O bonds. MTHF is a five-member ringed molecule that contains a hindered (tertiary) ^{3}C–O bond and an unhindered (secondary) ^{2}C–O bond (Fig. 1). Activating ^{3}C–O bonds in MTHF produces primary alcohol intermediates (1-pentanol), but similar chemistry can used to obtain higher-value chemicals, such as α,ω-diols.[12–16] Other molecules such as 2-(hydroxymethyl)tetrahydropyran or tetrahydrofurfuryl alcohol have similar tertiary carbons with

* Corresponding author.
E-mail address: hibbitts@che.ufl.edu (D. Hibbitts).

https://doi.org/10.1016/j.jcat.2023.02.011
0021-9517/

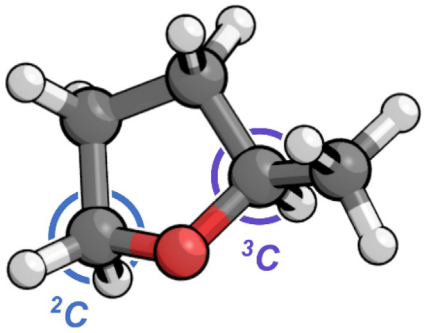

Fig. 1. MTHF molecule with highlighted secondary (^{2}C, blue) and tertiary carbon (^{3}C, purple) atoms. (For interpretation of the references to colour in this figure legend, the reader is referred to the web version of this article.)

hydroxymethyl substituents and can be formed into α,ω-diols with selective C–O hydrogenolysis.[9] Therefore, identifying catalysts that selectively cleave the hindered ^{3}C–O bond over the unhindered ^{2}C–O bond can improve the process of upgrading biomass to useful chemicals.

Metal phosphides (MPs) are promising catalysts for selective C–O bond activation. MPs were initially studied for the hydrodesulfurization and hydrodenitrogenation of fuels.[17–19] Many MPs, however, have also been shown to selectively cleave C–X (X = O, N, S) over C–C bonds in comparison to pure transition metals,[20–22] metal sulfides,[18,23] and metal nitrides.[24] More recently, MPs have also been shown to promote other reactions such as methanol steam reforming[25] and hydrogen evolution,[26] in addition to C–X hydrogenolysis. The selectivity and C–O activation rates on MPs are governed by the metal identity,[7,20,22,27,28] metal to phosphorous ratio,[21,28,29] formation of bimetallic phosphides,[30–33] and variations in the catalyst support.[34–36] Among MP catalysts, Ni_2P has been shown to be the most reactive towards the hydrogenolysis of C–O bonds in many oxygenates, including anisole,[30] guaiacol,[7,29,34,36,37] MTHF,[12–15,22,31] dibenzofuran,[28] and methyl laurate[32,35] when compared to NiMoP, MoP, Fe_2P, NiFeP, Co_2P, and WP catalysts.

The proposed reaction mechanism for C–O activation on MTHF assumes C–H activation to be facile, reversible, and to precede C–O activation. Experimental data suggests that the conversion between MTHF and methyl-furan (MF) is quasi-equilibrated leading to the assumption that the C–H activations on MTHF before C–O activation are also quasi-equilibrated.[16] This assumption is further supported through DFT calculations which show that C–H activations are more enthalpically favorable than C–O activations, C–H transition states have lower barriers than C–O barriers, at matching reaction coordinates. Also, free energy barriers for all possible C–O activations indicate that C–O activation through the fully dehydrogenated intermediate is the most favorable for both pathways. This mechanism of dehydrogenation before C–O activation has also been observed in many other studies investigating C–X (X = C, O, N, S) hydrogenolysis.[8,38–47].

Increasing P content on Ni_xP_y catalysts shifts selectivity toward ^{3}C–O activation. The underlying reasons, however, remain unclear. One explanation is that the addition of secondary components into metal catalysts may geometrically disrupt metal atom ensembles, altering their chemistry. For example, the incorporation of Sn in SnPt alloys disrupts Pt ensembles resulting in selectivity shifts during dehydrogenation reactions.[48–50] Zn and Ga influence the size and shape of Pd and Ni ensembles as intermetallic components that also alter reactivity.[51–54] The addition of a second component, however, may also modify the electronic density of the metal, as shown in DFT studies on layered metal models.[55] Therefore, selectivity shifts for C–O activation due to the incorporation of P into Ni could arise from changes in the geometry of the active sites, the electronic structure of the underlying material, or some combination of the two.

Structural inspection of Ni and Ni_2P transition states computed by DFT suggests that P does not participate in the chemistry, suggesting the role of P is to geometrically and electronically modify metal ensembles on transition metal phosphides (TMPs).[16] This is also suggested by the preferred adsorption of probe molecules such as H* and CH_3* to metal sites over P sites for a significant number of $M_2P(001)$ surfaces.[56] Measurements on rate inhibition by CO, H_2, and NH_3 indicate that both the ^{2}C–O and ^{3}C–O activations occur at the same active site and involve the same number of active sites. Visual inspection of DFT optimized Ni(111), $Ni_{12}P_5(001)$, and $Ni_2P(001)$ structures shows that the vast majority of the active sites for all of the reaction steps are comprised of Ni atom ensembles. Therefore, P does not directly take part in the chemistry for these reaction pathways.[16] However, this still does not answer the question as to how the addition of P causes the shifts in selectivity.

In this study, we explore C–O activation of MTHF on a broader set of isostructural transition metal (Fe, Co, Ru, Rh, Pd, Os, Ir, and Pt) phosphides to elucidate if the role of P on Ni_xP_y is ubiquitous and therefore present across other transition metal phosphides. Decoupling the geometric and electronic effects of adding P to Ni and other transition metals is crucial for tuning catalysts for the conversion of biomass-derived molecules into useful chemicals. We find that there is a nearly ubiquitous shift in selectivity towards the hindered (^{3}C–O) bond activation with the addition of P to the various transition metals investigated in this work. However, these shifts in selectivity do not always lead to an outright preference for ^{3}C–O activation. Given that the two materials that showed a preference for the hindered activation, Ni_2P and Pd_2P, both contain Group 10 metals, this shift in selectivity is likely caused by some combination of geometric and electronic effects. Also, periodic trends show that the Group 10 metals (Ni, Pd, Pt), have the highest activation barriers for C–O activation, but at the same time show the biggest shift in selectivity with the addition of P.

2. Computational methods

Periodic density functional theory (DFT) calculations were performed using the Vienna *ab initio* simulation package (VASP).[57–60] All calculations were implemented in the Computational Catalysis Interface (CCI).[61] The wavefunctions were constructed using plane waves with an energy cutoff of 400 eV, while the projector augmented wave (PAW) method was used to describe the wavefunctions in the core region.[62,63] The Perdew-Burke-Ernzerhof (PBE) form of the generalized gradient approximation (GGA) was used to determine exchange and correlation energies for bulk and surface formation.[64–66] The revised Perdew-Burke-Ernzerhof (RPBE) functional exhibits better performance in predicting adsorption energies on metal surfaces;[64–66] therefore, it was used for calculating adsorption, reaction, and activation energies on M(0001), M(111), and $M_2P(001)$ catalyst surface models used herein. In addition, the fast Fourier transforms (FFTs) were performed on either an untruncated FFT grid with twice the momentum cutoff used for expanding the wavefunctions or a truncated FFT grid with 1.5 × the momentum cutoff. Spin polarization was used for all pure Ni, Fe, and Co structures because they are ferromagnetic. Previous DFT studies showed that the energy difference between spin- and non-spin-polarized calculations for $Ni_{12}P_5(001)$ and $Ni_2P(001)$ structures was < 10^{-4} eV.[67] Therefore, all M_2P calculations were done without spin polarization.

Gaseous species were modeled within 16 × 16 × 16 Å unit cells of vacuum.

2.1. Bulk and surface formations

We extend our prior work on Ni(1 1 1) and Ni_2P(0 0 1) by examining M(1 1 1) or (0 0 0 1) pure metal surfaces (depending on whether they are FCC or HCP, respectively) and comparing their selectivities to their respective M_2P structure that is *iso*-structural to Ni_2P(0 0 1). The unit cells of bulk Ni (space group *Fm* $\bar{3}$ *m*)[68] and Ni_2P (space group *P* $\bar{6}$ 2 *m*)[69] were built from crystallographic data and then both the atomic coordinates and lattice parameters were optimized using DFT. The optimized bulk lattice parameters for Ni ($a = b = c = 3.52$ Å) and Ni_2P ($a = b = 5.87$ Å and $c = 3.37$ Å) were in close agreement with the measured values ($a = b = c = 3.52$ Å for Ni[68] and $a = b = 5.86$ Å, $c = 3.38$ Å for Ni_2P)[70] and were consistent with previous DFT studies.[67] The M_2P bulk structures were constructed by substituting Ni for the metal of interest in the optimized Ni_2P bulk structure (further details are in Section S1.1 of the SI), and the atomic coordinates and lattice parameters were optimized. Geometries of these bulk structures were optimized until the maximum force on each atom was < 0.01 eV $Å^{-1}$ and the wavefunctions were converged to within 10^{-8} eV. K-point meshes of 12 × 12 × 12 and 20 × 20 × 35 were used for the pure metals and metal phosphides, respectively, during bulk structure optimization. The energies at these K-point meshes changed by less than 1×10^{-2} eV at larger *k*-points, as further detailed in the SI (Section S1.2).[16] The lattice parameters for these bulk structures were allowed to optimize. Bulk formation energies ($E_{form,b}$) were then calculated using these optimized energies along with the balanced chemical formula with the pure metal, phosphine (PH_3), and gaseous hydrogen (H_2). If a material significatly restructured during the bulk optimization calculations, it was excluded from any subsequent parts of this study as was the case with Os_2P, Ir_2P and Pt_2P. The structures were cleaved to form slab-models from the highest k-point mesh from the bulk material calculations.

Surfaces were cut from the corresponding optimized bulk structures and further optimized while fixing the bottom two layers to their bulk positions. Pure metal surfaces were modeled as 3 × 3 close-packed periodic lattices with four layers in the orthogonal direction and a 10 Å vacuum between slabs. For FCC metals, the (1 1 1) surfaces were used, while for HCP metals, the (0 0 0 1) surface was used as these are most isostructural to Ni (1 1 1). In the case of Fe, which is typically a BCC metal, an HCP (0 0 0 1) structure was used to maintain the *iso*-structural component of this investigation, because BCC metals lack a surface isostructural to Ni(1 1 1). So, for the context of this study we put Fe in the HCP (0 0 0 1) (with optimized lattice parameters) to maintain that structure.

For Ni_2P surfaces, there is an alternation of planes in the *z* direction that have different Ni and P compositions; scanning tunneling microscope (STM) images show the existence of two different terminations on Ni_2P(0 0 1) single crystals.[71] DFT calculations suggest that the Ni-rich termination in Ni_2P (0 0 1) has the lowest surface formation energy by approximately 1.04 eV nm^{-2} and about 0.52 eV nm^{-2} in comparison to the next lowest Miller index for Ni_2P.[16] Therefore, the Ni-rich Ni_2P(0 0 1) surface was used. In the interest of this *iso*-structural investigation, M_2P surfaces were constructed to match this Ni-rich Ni_2P(0 0 1) surface. The M_2P (0 0 1) surfaces were modeled with 10 Å vacuum in the *z* direction and two repeating units. The layers in the bottom half of each slab were fixed at their bulk positions during geometry optimization. Using these DFT calculated energies, surface formation energies for each of the phosphides were determined.

Surfaces were optimized in three steps, the first step for this process had wavefunctions converge to within 10^{-4} eV and forces were calculated using a truncated FFT grid. The second step had wavefunctions converge to within 10^{-6} eV and forces were calculated using an untruncated FFT grid. Both steps converged after the maximum force on each atom was < 0.05 eV $Å^{-1}$.[61] Lastly, for the pure metals, a single point calculation was performed using an enlarged mesh (8 × 8 × 1) with the same wavefunction criteria as the first step. These settings, including the PBE exchange–correlation functional, were used to calculate bulk and surface formation energies.

2.2. Energy barrier calculations

Adsorption, reaction, and activation energies were calculated using the RPBE functional. These structures were optimized using a multi-step process (two-step for M_2P surfaces, three-step for M surfaces) which has been demonstrated to be ~ 7 × faster than a single step calculation for surfaces.[61] Wavefunctions were converged to within 10^{-4} eV using a truncated FFT grid for Step 1 and 10^{-6} eV using an untruncated FFT grid for Step 2. Structures were relaxed until all forces on unconstrained atoms were < 0.1 eV $Å^{-1}$ in Step 1 and < 0.05 eV $Å^{-1}$ in Step 2. For both steps, *k*-points meshes of 4 × 4 × 1 and 5 × 5 × 1 were used for the metal and M_2P surfaces, respectively. After geometric convergence, the electronic energy was determined by using a single-point calculation with an 8 × 8 × 1 *k*-point mesh and a wavefunction convergence of 10^{-4} eV.

The nudged elastic band (NEB) method[72,73] and the Dimer method[74] were used to obtain transition-state structures. The NEB method was carried out using 16 images. Wavefunctions were converged to within 10^{-4} eV and the maximum force was converged to < 0.5 eV $Å^{-1}$ on each atom. This provides a rough estimate of the minimum energy pathway and provides initial guesses of transition state structures and reaction modes used in the Dimer method. Then the Dimer algorithm was used with wavefunctions converged to within 10^{-6} eV and the maximum force converged to < 0.05 eV $Å^{-1}$ on each atom.

Vibrational frequency calculations were done for all catalytic intermediates and transition states using a finite difference method where atoms in all adsorbate structures were displaced by 0.015 Å in each direction to calculate the Hessian matrix. Vibrational frequencies are used to estimate zero-point vibrational energy (ZPVE) and temperature corrected enthalpies (*H*) and free energies (*G*) (More details provided in Section S1 of the SI).

2.3. Charge analysis calculations

Partial charges were computed using the quasiatomic orbital (QO) method developed by Qian *et al.*[75] and implemented into the VASP code by Plaisance *et al.*[76] The quasiatomic orbitals generated by this method resemble valence atomic orbitals of free atoms, but are slightly distorted so that they are able to exactly reproduce all occupied bands in the ground state. This yields a convenient tight binding basis for constructing the population matrix. Once the population matrix is constructed in the QO basis, a Löwdin population analysis is performed to compute the partial atomic charges. In contrast to Bader charge analysis, the QO charges are associated with specific orbitals and thus have a more fundamental chemical interpretation, as described further in prior work.[76].

3. Results and discussion

3.1. Ni and Ni_2P overview

Our previous work has shown that both secondary and tertiary C–O activations in MTHF occur after complete dehydrogenation of the C-atom and that C–H activations on MTHF are facile and reversible over Ni and Ni_xP_y catalysts.[16,38] Kinetic measurements during MTHF hydrogenolysis show equilibrated amounts of methylfuran formed across a wide range of space velocities on 4 nm Ni, 5 and 19 nm $Ni_{12}P_5$, and 12 nm Ni_2P catalysts. This suggests that C–H readily activates on MTHF over Ni and Ni_xP_y catalysts, irrespective of P content.[16] A reaction scheme that assumes ^{2}C–O and ^{3}C–O activation are preceded by quasi-equilibrated dehydrogenation steps was proposed,[16] starting with the quasi-equilibrated dissociative adsorption of H_2 and the adsorption of MTHF (Eqs. (1), and 2 respectively):

$$H_2(g) \rightleftharpoons 2H^* \tag{1}$$

$$C_5H_{10}O(g) \rightleftharpoons C_5H_{10}O^* \tag{2}$$

After MTHF adsorption, two dehydrogenation steps (Eqs. (3) and (4)) precede the ^{2}C–O activation step (Eq. (5)),

$$-R-O^*-CH_2 -+ * \rightleftharpoons -R-O^*-CH^*- + H^* \tag{3}$$

$$-R-O^*-CH^*- + * \rightleftharpoons -R-O^*-C^*- + H^* \tag{4}$$

$$-R-O^*-C^*- + * \rightleftharpoons C^*-R-O^* \tag{5}$$

where R represents the portion of the ring ($-CH_2CH_2CH(CH_3)-$) that does not directly participate in any of the steps related to ^{2}C–O activation. Only one dehydrogenation step (Eq. (6)) precedes the ^{3}C–O activation (Eq. (7)),

$$-R'-O^*-CH(CH_3) - + * \rightleftharpoons -R'-O^*-C^*(CH_3) - + H^* \tag{6}$$

$$-R'-O^*-C^*(CH_3) - + * \rightleftharpoons H_3C-C^*-R-O^* \tag{7}$$

where R′ represents the portion of the molecule ($-CH_2CH_2CH_2-$) that does not directly participate in any of the steps related to ^{3}C–O activation. The C–O activations for each pathway are the rate limiting (kinetically relevant) steps following complete dehydrogenation. The recombinative desorption of H* (to form H_2) is assumed to be quasi-equilibrated and therefore kinetically irrelevant in this study.

Turnover rates (rates per site, L) for both ^{2}C–O and ^{3}C–O activation are proportional to the concentration of the MTHF-derived reactive intermediates for their respective pathways (Eqs. (5) and (7)):

$$\frac{r_{mC-O}}{[L]} = \frac{k_{mC-O}[C_5H_{6+m}O^*]}{[L]} \tag{8}$$

where m is either 2 or 3 for ^{2}C–O and ^{3}C–O activation, respectively. Treating adsorption and dehydrogenation steps as quasi-equilibrated, these rate equations can be rewritten in terms of the concentrations of MTHF and H_2 reactants:

$$\frac{r_{2C-O}}{[L]} = k_5K_4K_3K_2[\mathrm{MTHF}]\cdot(K_1[H_2])^{-1}\left(\frac{[*]}{[L]}\right) \tag{9a}$$

$$\frac{r_{3C-O}}{[L]} = k_7K_6K_2[\mathrm{MTHF}]\cdot(K_1[H_2])^{-1/2}\left(\frac{[*]}{[L]}\right) \tag{9b}$$

where rate (k) and equilibrium (K) constants are defined by their corresponding reaction step equation in Equations (1)–(7). The lumped rate and equilibrium constants in Equations 9 can be defined for ^{2}C–O and ^{3}C–O activation:

$$k_{eff,2} = k_5K_4K_3K_2K_1^{-1} \tag{10a}$$

$$k_{eff,3} = k_7K_6K_2K_1^{-0.5} \tag{10b}$$

and these effective rate constants are related to the free energies to form the ^{2}C–O and ^{3}C–O activation transition states relative to a bare catalyst surface:

$$k_{eff} = \frac{k_bT}{h}e^{\frac{\Delta G^\ddagger}{RT}} \tag{11}$$

These effective barriers ($\Delta H^\ddagger$ and $\Delta G^\ddagger$) are defined as the enthalpy or free energy of forming the transition state $[C_5H_{(10-\lambda/2)}O^*{}^\ddagger]$ and a stoichiometric amount of gas-phase H_2 from gas-phase MTHF ($C_5H_{10}O$) and a bare surface:

$$C_5H_{10}O(g) + * \rightarrow \left[C_5H_{(10-\lambda/2)}O*\right]^\ddagger + \lambda H_2(g) \tag{12}$$

$$\Delta H^\ddagger = H^\ddagger + \lambda H_{H_2} - H_{MTHF} - H_* \tag{13}$$

$$\Delta G^\ddagger = G^\ddagger + \lambda G_{H_2} - G_{MTHF} - G_* \tag{14}$$

These effective barriers are distinct from DFT-derived intrinsic enthalpy and free energy barriers (ΔH_{act} and ΔG_{act}, respectively) and reaction energies (ΔH_{rxn} and ΔG_{rxn}) which denote differences between a transition state or the product and the respective catalytic intermediate preceding each elementary step. Critically, this work focuses on selectivity, described here as $\chi = \frac{r_{3C-O}}{r_{2C-O}}$, and this ratio can be written in terms of effective rate constants and reactant concentrations:

$$\chi = \frac{r_{3C-O}}{r_{2C-O}} = \frac{k_{eff,3}}{k_{eff,2}}[H_2]^{1/2} \tag{15}$$

The corresponding rate expressions for ^{2}C–O (Eq. (9a)) and ^{3}C–O (Eq. (9b)) activation in MTHF differ by a half-order dependence in H_2 pressure, reflecting differences in the number of C–H activations that precede each C–O activation. Kinetic measurements on the ratio of ^{2}C–O and ^{3}C–O activation rates as a function of hydrogen pressure showed that the ratio varies with $(H_2)^{1/2}$ across all Ni_xP_y catalysts,[16] consistent with the proposed mechanism (Eq. (15)). Furthermore, rate measurements show that the rates for ^{2}C–O and ^{3}C–O activations are equally inhibited by site-blocking due to co-fed CO and NH_3;[16] this suggests that secondary and tertiary C–O activations occur on the same active sites and require the same number of those active sites on the catalyst surface. This rate-ratio (χ) can be related to a difference in effective free energy barriers ($\Delta G^\ddagger$), described here as $\Delta\Delta G$:

$$\chi = e^{\frac{\Delta\Delta G}{RT}} \tag{16}$$

$$\Delta\Delta G = \Delta G^\ddagger_{2C-O} - \Delta G^\ddagger_{3C-O} \tag{17}$$

Here, we summarize our past work on Ni(1 1 1) and Ni_2P(0 0 1) surfaces to contextualize the present study of other metals and metal phosphides. Activation of C–H on MTHF occurs with lower barriers than C–O activation in intermediates in which the C in the activated C–O bond is not fully dehydrogenated, consistent with the proposed mechanism. Enthalpic barriers for C–O activation (ΔH_{act}) in MTHF and partially dehydrogenated intermediates were estimated by DFT to be larger than the corresponding C–H activations (Fig. 2). For example, ΔH_{act} is 70 kJ mol^{-1} for the first dehydrogenation step of ^{2}C–O activation on Ni(1 1 1) versus 155 kJ mol^{-1} to activate the C–O bond directly (Fig. 2). This difference in preference is observed for both ^{2}C–O and ^{3}C–O activations on both Ni(1 1 1) and Ni_2P(0 0 1) surfaces.

C–O activations in MTHF and partially dehydrogenated intermediates differ in the number of the stoichiometrically formed H_2(g), and hence they differ significantly in their activation entro-

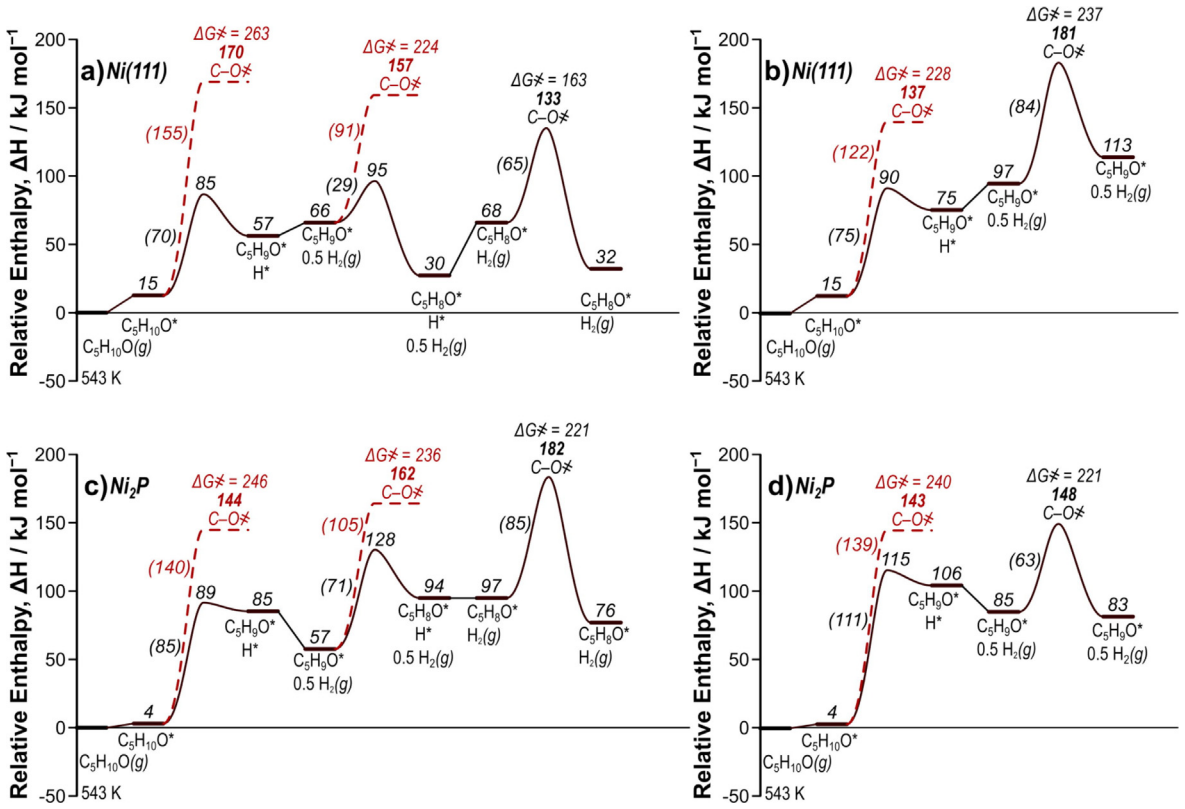

Fig. 2. Reaction coordinate diagrams showing enthalpies (ΔH) in kJ mol^{-1} relative to the bare surface and gas phase MTHF at 543 K for (a,c) the ^{2}C–O bond activation and (b,d) the ^{3}C–O bond activation. Enthalpies are shown for reactions on (a–b) Ni(1 1 1) and (c–d) Ni_2P(0 0 1). The solid black lines indicate the preferred reaction pathway through the fully dehydrogenated intermediate. The dashed red lines indicate alternate pathways where a C–O bond is activated before full dehydrogenation. Each state is labeled with its enthalpy and transition states are labeled with their overall free energies of activation ($\Delta G^{\ddagger}$) in kJ mol^{-1}. The intrinsic activation barriers (ΔH_{act}) are provided in parentheses for each reaction step. (For interpretation of the references to colour in this figure legend, the reader is referred to the web version of this article.)

pies. As such, enthalpy becomes an inadequate descriptor to compare these various C–O activations. Therefore, we compare these pathways by using the overall activation free energies ($\Delta G^{\ddagger}$, Fig. 2), which include these entropic contributions. The free energy barriers for the fully dehydrogenated pathway are lower than those for the other C–O activations, with the exception of ^{3}C–O activation on Ni(1 1 1), indicating that the fully dehydrogenated C–O activation pathway is the most favorable. These data suggest that the mechanism occurs as described in Equations (1)–(7). Hence, we will use a similar DFT analysis in this work to examine additional pure metal and M_2P surfaces isostructural to Ni and Ni_2P.

The ratio of rates (χ) of product formation for Equations (5) and (7) (Eq. (15)), as measured experimentally, serves to describe the selectivity of secondary to tertiary C–O activation. Kinetic measurements of C–O activation in MTHF (473–575 K, 5 kPa MTHF, 1 MPa H_2) show that values of χ increase with increasing P content (~0.1 for Ni, ~0.5 for $Ni_{12}P_5$, and ~ 3 Ni_2P), suggesting that incorporation of P systematically shifts selectivity towards ^{3}C–O activation.[16] This is supported by DFT estimates of the enthalpic barriers for fully dehydrogenated secondary and tertiary C–O bond activation. On Ni(1 1 1) surfaces, activation of the ^{2}C–O bond ($\Delta H^{\ddagger}$ = 133 and $\Delta G^{\ddagger}$ = 163 kJ mol^{-1}) occurs with lower barriers than activation of the ^{3}C–O bond ($\Delta H^{\ddagger}$ = 181 and $\Delta G^{\ddagger}$ = 237 kJ mol^{-1}). On Ni_2P in contrast, activation of the ^{3}C–O bond ($\Delta H^{\ddagger}$ = 148 and $\Delta G^{\ddagger}$ = 221 kJ mol^{-1}) occurs with a lower $\Delta H^{\ddagger}$ barrier and equal $\Delta G^{\ddagger}$ barrier than activation of the ^{2}C–O bond ($\Delta H^{\ddagger}$ = 182 and $\Delta G^{\ddagger}$ = 221 kJ mol^{-1}). The preference for the cleavage of the ^{2}C–O bond over the ^{3}C–O bond can be described by differences in activation energies,

$$\Delta\Delta H = \Delta H^{\ddagger}_{2C-O} - \Delta H^{\ddagger}_{3C-O} \quad (18)$$

where a positive $\Delta\Delta H$ or $\Delta\Delta G$ (Eq. (17)) value indicates a preference toward ^{3}C–O bond activation. Ni and Ni_2P have $\Delta\Delta H$ values of −48 and 34 kJ mol^{-1} and $\Delta\Delta G$ of −70 and 0 kJ mol^{-1} respectively, suggesting that Ni_2P more selectively activates the ^{3}C–O bond over the ^{2}C–O, in agreement with experimental observations.[16] Further, the $Ni_{12}P_5$ surface studied in our previous work had a $\Delta\Delta H$ value (543 K) of 11 kJ mol^{-1} and $\Delta\Delta G$ value of −13 kJ mol^{-1}, indicating selectivity falling between that of Ni and Ni_2P, as observed experimentally.[16] These $\Delta\Delta H$ and $\Delta\Delta G$ values for NiP_x accurately predict the trend of increasing ^{3}C–O activation selectivity with increasing P content and will be used here to predict selectivities in materials that have not yet been synthesized or tested to determine whether the effect of P incorporation is ubiquitous across a series of transition metals.

3.2. Selection of other transition metal phosphides

The underlying reasons for the observed trends in selectivity toward ^{3}C–O bond activation with P incorporation in Ni_xP_y remains undetermined. In most cases, the P atoms do not directly participate in the chemistry in either C–H or C–O activation reactions in reactions on Ni_2P, rather most adsorption and reaction steps take place over P-modified metal ensembles.[16] Shifts in selectivity could be caused by either P altering the electronic nature of these metal ensembles (e.g., creating positively charged Ni atoms), or by altering their geometric arrangement or distribution (e.g., breaking up extended M domains). Here, we extend our understanding of Ni and Ni_2P catalysts by investigating the MPs of other

transition metals and comparing them to their respective pure metal surfaces.

There are many transition metal phosphide materials that have been synthesized, but few that match the structure and composition of Ni_2P. We considered the Material Project[77] database and Crystallography Open Database (COD)[78–83] for all of the Groups 8–10 transition metals in rows 4–6 on the periodic table (Fe, Ni, Co, Ru, Rh, Pd, Os, Ir, and Pt). These metals all have known phosphide crystal structures, ranging from high P content in FeP_4 and RuP_4 (80 mol% P) to low P content in $Pd_{15}P_2$ (11 mol% P). While most metals have been synthesized in the M_2P stoichiometry, no M_2P material has been synthesized for Pd, Os, or Pt (Table 1). [84–89] Furthermore, even for metals that have been reported with M_2P stoichiometry, they often exhibit different bulk structures from Ni_2P. Indeed, only Fe_2P exists in the same space group ($P\bar{6}2m$) as Ni_2P (Table 1, Fig. 3a,c);[90–92] Co_2P[93–97] and Ru_2P[98] exist in the *Pnma* space group (Fig. 3e,g), while Rh_2P [99] and Ir_2P[100] are in the $Fm\bar{3}m$ space group (Fig. 3i,k). These structural differences render it challenging to decouple geometric from electronic effects within these materials.

We circumvent this challenge by constructing theoretical models for bulk M_2P structures that are initially isostructural to Ni_2P ($P\bar{6}2m$ space group), followed by optimization of the atom positions and lattice parameters. Bulk models for Os_2P, Ir_2P, and Pt_2P significantly restructured during optimization. In Ni_2P, the metal atoms coordinated with each P atom tend to form a triangular shape around the P atom from a top-down view (Fig. 3b). However, a hexagonal shape was formed around the P atoms for Os_2P, Ir_2P, and Pt_2P (Fig. 3l,o,p). Therefore, these three M_2P structures of row 6 metals were excluded from further investigation, while those composed of metals in rows 4–5 were examined for C–O hydrogenolysis reactivity. Another option would have been to constrain the Os, Ir, and Pt-based structures to match that of Ni_2P, but we believe that modeling constrained surfaces can give misleading results for the chemistry.

The stability of the theoretical structures was examined using bulk and surface formation energies. The bulk formation energy ($\Delta E_{form,b}$) was calculated across all theoretical structures with respect to the corresponding pure bulk metals along with gas-phase phosphine (PH_3) and H_2,

$$\Delta E_{form,b} = \upsilon_{H_2} E_{H_2} + \upsilon_{M_6P_3} E_{M_6P_3} - \upsilon_{PH_3} E_{PH_3} - \upsilon_{M_{bulk}} E_{M_{bulk}} \quad (19)$$

where υ_x are stoichiometric coefficients. The $\Delta E_{form,b}$ values for Co_2P, Fe_2P, Pd_2P, Rh_2P, and Ru_2P are relatively close to Ni_2P (within $\sim$ 40 kJ $mol^{-1}P^{-1}$) (Table 2). Meanwhile, Pt_2P, Ir_2P, and Os_2P (the bulk systems that restructured) have significantly less negative $\Delta E_{form,b}$ values than Ni_2P, rationalizing their restructuring and exclusion from further investigation.

Bulk structures were cleaved to form $M_2P(001)$ surfaces, matching the low energy surface for Ni_2P. From these, surface formation energies ($\Delta E_{form,s}$) were calculated using,

$$\Delta E_{form,s} = (E_{surf} - \upsilon E_{bulk})/(2A_{surf}) \quad (20)$$

where E_{surf} and E_{bulk} are the surface and bulk optimized energies of each, υ (N_{surf}/N_{bulk}, N being number of atoms) is a stoichiometric factor, A_{surf} is the surface cross-sectional area of the top of the slab, and the factor of 2 corresponds to the formation of both a bottom and top surface in the slab models. Values for $\Delta E_{form,s}$ across the examined M_2P surfaces, are within ± 8 eV nm^{-2} of that for Ni_2P (Table 2). This suggests that these M_2P surfaces are not unrealistic or under significant strain and can be further examined to deconvolute electronic from geometric effects that arise from adding P to transition metal surfaces during C–O hydrogenolysis. In this study, because we are looking at these isostructural materials, the geometric effects of adding P to each of the transition metals will be quite similar. As such, the results from this study will emphasize electronic factors that may result in shifting the selectivity of C–O hydrogenolysis with the addition of P.

3.3. Reaction mechanism on other metal and metal phosphide surfaces

MTHF hydrogenolysis pathways were examined on the other Pt-group metals (Fe, Co, Ru, Rh, Pd, Os, Ir, Pt) and metal phosphides (Fe_2P, Co_2P, Ru_2P, Rh_2P, Pd_2P). The phosphides of Pt, Ir, and Os phosphides were excluded from this study after the bulk material calculations showed significant restructuring compared to Ni_2P (Section 3.1), although the pure metals are still included in the analysis of periodic trends (Section 3.6). For this isostructural study, HCP Fe was used rather than the more stable BCC crystal structure since the latter does not have a close-packed surface that matches the Ni (1 1 1) surface; hence the Fe HCP(0001) surface was used instead.

The general mechanism on all surfaces (metals and metal phosphides) for C–O hydrogenolysis is analogous to the mechanism found on Ni and Ni_2P. As seen in Fig. 4 for Co and Co_2P, in Fig. 6 for Pd and Pd_2P, and Figures S3–S7 in the Supporting Information for the other surfaces, the relative activation enthalpies of all C–H activation steps are lower than the corresponding C–O activation steps from the same intermediate. In other words, the activation barrier is always lower to dehydrogenate the carbon atom than to cleave the C–O bond until the carbon atom is fully dehydrogenated. Furthermore, the transition state for C–O activation from the fully dehydrogenated intermediate has a lower free energy than C–O activation transition states from intermediates earlier along the reaction pathway. Therefore, it can be concluded that hydrogenolysis generally occurs by full dehydrogenation of the carbon atom followed by kinetically relevant C–O cleavage.

In addition, it is found that the reaction intermediates of both the ^{2}C–O and ^{3}C–O hydrogenolysis pathways bind to the M_2P sur-

Table 1
Summary of all the metal phosphides investigated in this study and whether similar materials have been studied in terms of composition and preferred crystalline structure (space group).

Metal	Row	Column	Synthesized Phosphide Stoichiometries	M_2P Space Group
Fe	4	8	FeP_4, FeP_2, FeP, **Fe_2P**, Fe_3P, Fe_4P	$P\bar{6}2m$
Co	4	9	CoP_3, CoP_2, CoP, $Co_{12}P_7$, **Co_2P**, Co_3P	*Pnma*
Ni	4	10	NiP_4, NiP_3, NiP_2, NiP, Ni_5P_4, **Ni_2P**, $Ni_{12}P_5$, Ni_8P_3, Ni_3P	$P\bar{6}2m$
Ru	5	8	RuP_4, RuP_3, RuP_2, RuP, **Ru_2P**	*Pnma*
Rh	5	9	Rh_4P_3, **Rh_2P**	$Fm\bar{3}m$
Pd	5	10	PdP_3, PdP_2, Pd_7P_3, Pd_3P, Pd_4P, Pd_6P, $Pd_{15}P_2$	–
Os	6	8	OsP_4, OsP_2	–
Ir	6	9	IrP_3, IrP_2, **Ir_2P**	$Fm\bar{3}m$
Pt	6	10	PtP_2, Pt_5P_2, Pt_3P	–

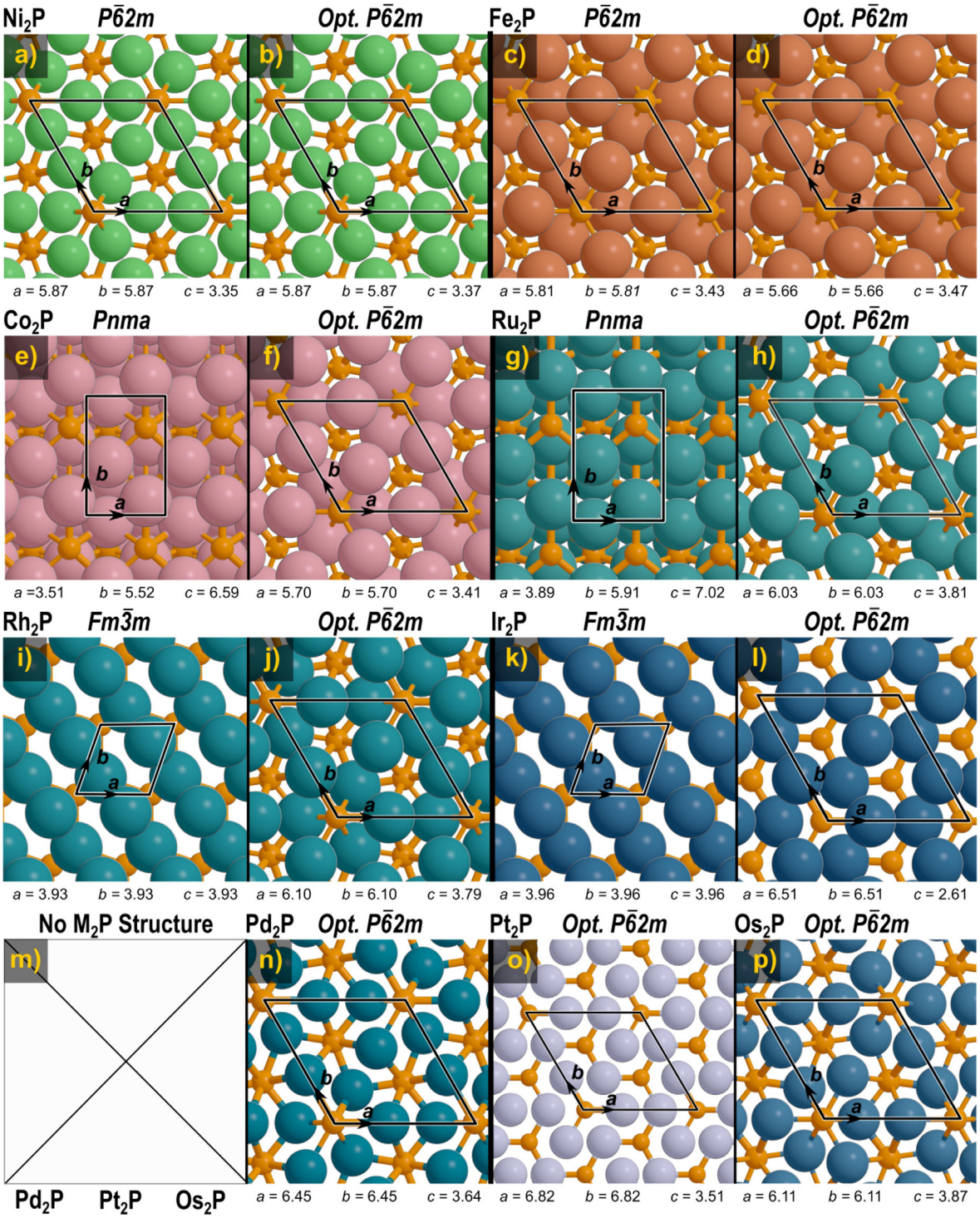

Fig. 3. The known bulk M_2P structures for Pt-group metals (a,c,e,g,i,k,m,o) and the theoretical bulk structures created for the purposes of this study (b,d,f,h,j,l,n,p). No M_2P structure has been synthesized, in any space group, for Pd, Os, or Pt phosphides. Above the known structures the space group for each structure is given.

Table 2
Bulk (kJ mol^{-1}) and surface (eV nm^{-2}) formation energies for all of the transition metal phosphides calculated using Equations (19) and (20) respectively.

	Fe_2P	Co_2P	Ni_2P	Ru_2P	Rh_2P	Pd_2P	Os_2P	Ir_2P	Pt_2P
Bulk	−261	−313	−284	−230	−292	−246	−100	−169	−191
Surface	16	13	9	14	9	5	N/A[a]	N/A[a]	N/A[a]

[a] These surfaces do not have surface formation energies because their bulk models restructured during optimization.

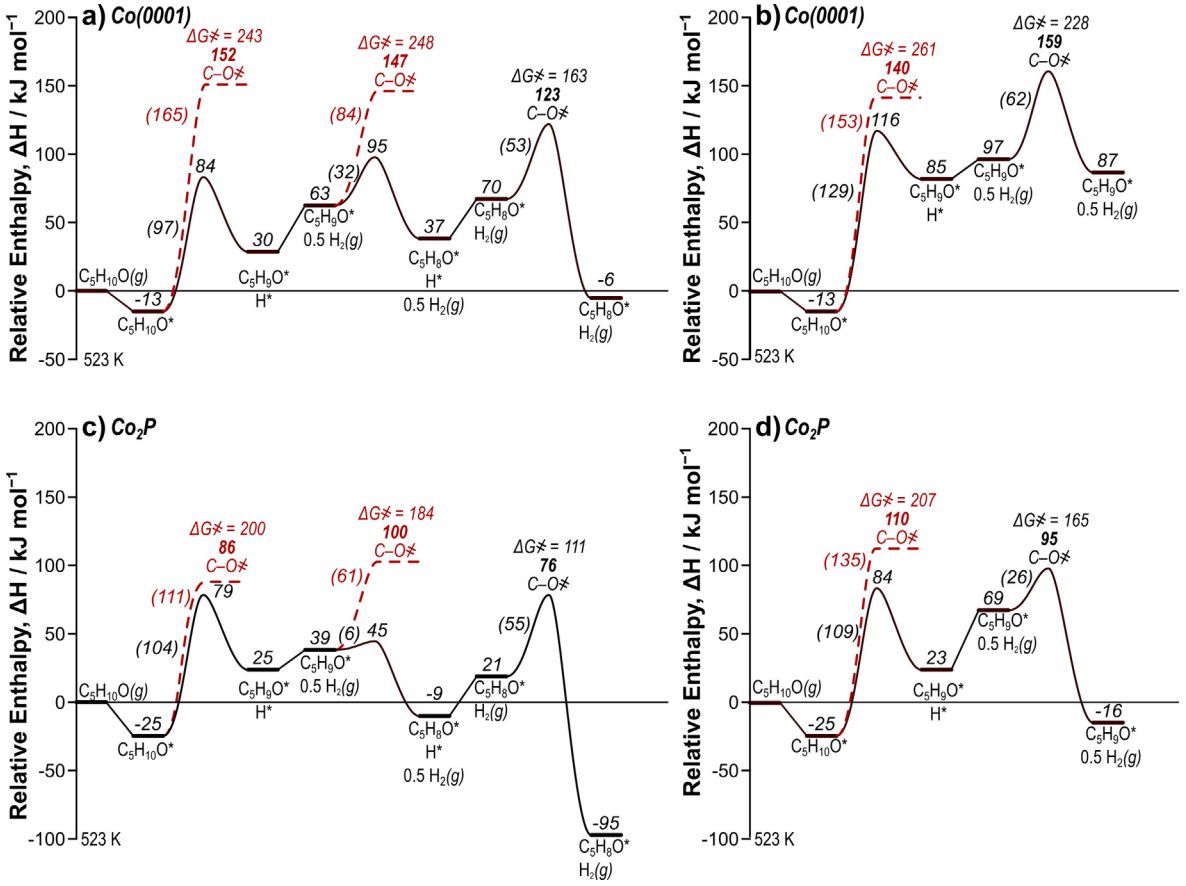

Fig. 4. Reaction coordinate diagrams relative to the bare surface and gas phase MTHF at 523 K for Co(0001) for the ^{2}C–O bond activation (a) and the ^{3}C–O bond activation (b) along with the reaction coordinate diagrams for Co_2P(001) for the ^{2}C–O bond activation (c) and the ^{3}C–O bond activation (d). The solid black lines indicate the main (fully dehydrogenated) reaction pathway. The dashed red lines indicate alternate pathways where a C–O bond is activated before full dehydrogenation. The red and black numbers correspond to the relative enthalpies of their respective reactant, product, or transition state. The intrinsic activation barriers (ΔH_{act}) are provided in parentheses for each reaction step. (For interpretation of the references to colour in this figure legend, the reader is referred to the web version of this article.)

face in a similar configuration as on Ni_2P (Fig. 5). A similar configuration is also found for the pure metal surfaces compared to Ni (Fig. S22). Therefore, the active sites on all additional surfaces should resemble, at least geometrically, those on Ni and Ni_2P. These similarities among surfaces suggest that there are no artifacts associated with differences in mechanisms or active sites between the models; therefore, DFT models can elucidate the role of P in Ni_2P and other transition metal phosphides through the decoupling of electronic and geometric effects.

3.4. Selectivity shift between Co and Co_2P

The DFT-calculated transition state formation enthalpies ($\Delta H^{\ddagger}$) and free energies ($\Delta G^{\ddagger}$) on Co(0001) are similar to the corresponding values on Ni(111) surfaces (Figs. 2 and 4). In contrast, the $\Delta H^{\ddagger}$ and $\Delta G^{\ddagger}$ values are much lower on Co_2P(001) than on Ni_2P(001) for both ^{2}C–O and ^{3}C–O activation. While one could surmise that Co_2P(001) surfaces would be more reactive than Ni_2P(001) surfaces, should the former be investigated experimentally, it is important to remember that these $\Delta H^{\ddagger}$ and $\Delta G^{\ddagger}$ values reflect barriers to form ^{2}C–O and ^{3}C–O activation transition states from bare catalyst surfaces. In reality, both Co_2P(001) and Ni_2P(001) surfaces are expected to be covered (in part or fully) by strongly bound site-blocking intermediates, such as CO* formed from decarbonylation of ring-opened products.[16] Accurate prediction of turnover rates among both metal and metal-phosphide surfaces would first require determination of the most abundant surface intermediates (MASI) under reaction conditions along with calculation of the energies required to desorb such species to make room for C–O activation transition states. Such predictions are most useful alongside measured kinetic data that can give insights into the identity of MASI, as done in prior work on NiP_x, but is outside our immediate attention.[16] Instead, this work is focused on how P incorporation impacts the selectivity, or relative rates, of ^{2}C–O and ^{3}C–O activation. These relative rates are, fortunately, independent of the MASI as shown by CO cofeeds at different pressures (thus varying CO*, MTHF*, and H* coverages). The presence of such MASI equally inhibited ^{2}C–O and ^{3}C–O rates without impacting the ratio (χ) between them. These selectivities (χ) on Ni and NiP_x surfaces were shown to correlate with calculated $\Delta\Delta H$ and $\Delta\Delta G$ values (Eqs. (11) and (12)), which accurately predict shifts in selectivity with P incorporation in NiP_x materials, as described in Section 3.1. [16].

The addition of P to Co causes a shift in selectivity towards ^{3}C–O activation, but less significant than the shift observed for the addition of P to Ni. The $\Delta\Delta G$ value for Co(0001) is −65 kJ mol^{-1}, suggesting that the pure Co surface is selective towards the unhindered ^{2}C–O activation. This is consistent with trends reported for Ni(111) ($\Delta\Delta G$ value of −70 kJ mol^{-1}), indicating very similar selectivities would be observed for Co and Ni, and their similar $\Delta\Delta H$ values indicate this would be true across a range of temperatures. The $\Delta\Delta G$ value for Co_2P(001) is −54 kJ mol^{-1}, in contrast to Ni_2P(001) for which the $\Delta\Delta G$ is 0 kJ mol^{-1}. So, unlike Ni_2P, we expect that Co_2P would preferentially cleave ^{2}C–O bonds in MTHF. Other studies have shown that it is not unusual for Co_2P to be less selective than Ni_2P for C–O hydrogenolysis[7] and other

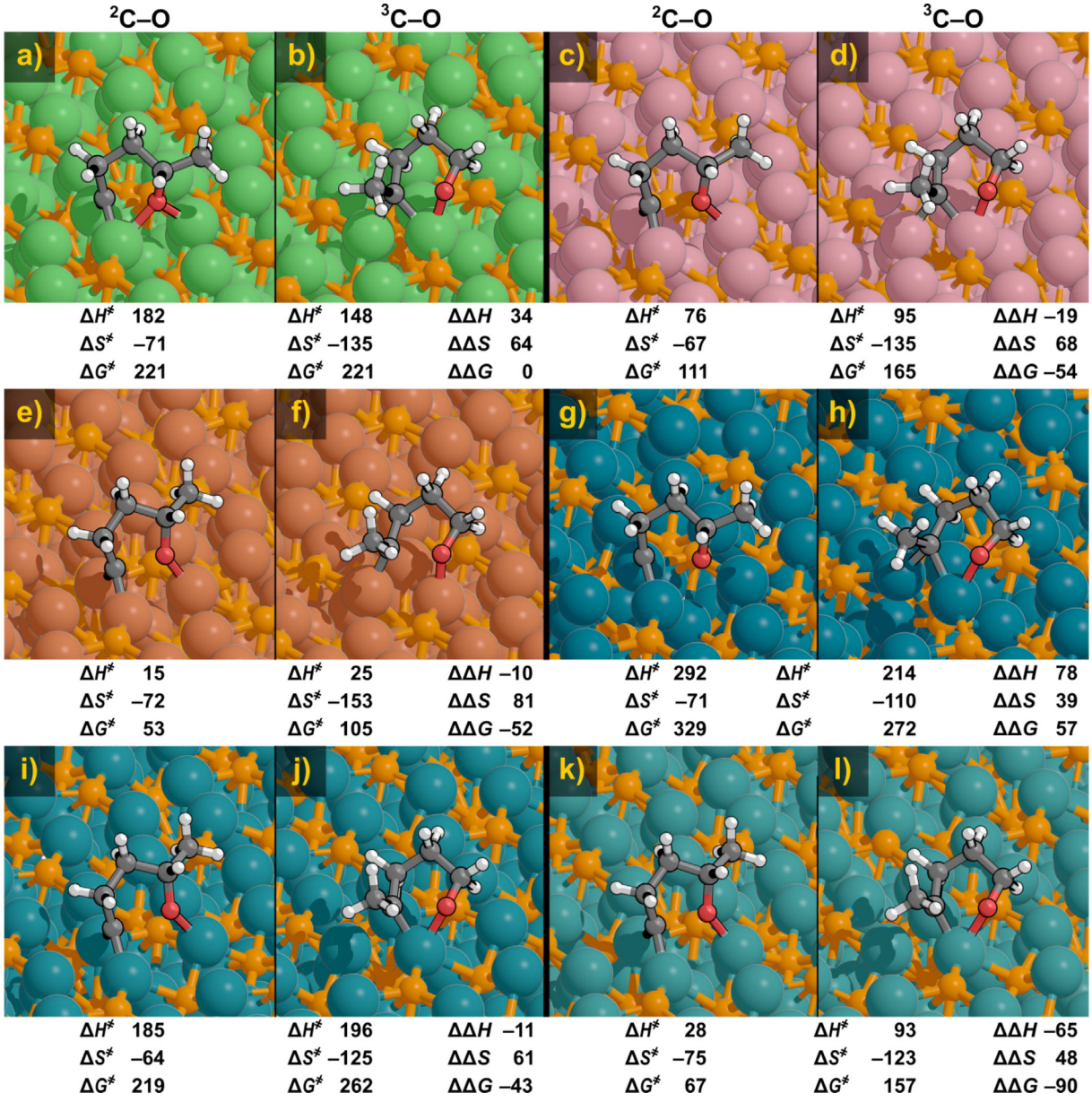

Fig. 5. Transition state structures for C–O activation on Ni_2P (a-b), Co_2P (c-d), Fe_2P (e-f), Pd_2P (g-h), Rh_2P (i-j), and Ru_2P (k-l) for both ^{2}C–O (a,c,e,g,i,k) and ^{3}C–O (b,d,f,h,j,l) activations. Also, listed are the $\Delta H^{\ddagger}$ (kJ mol^{-1}), $\Delta G^{\ddagger}$ (kJ mol^{-1}), and $\Delta S^{\ddagger}$ (J mol^{-1} K^{-1}). The differences between the ^{2}C–O and ^{3}C–O for these values are also provided in the form of $\Delta\Delta H$, $\Delta\Delta S$, and $\Delta\Delta G$.

reactions such as hydrodesulfurization and hydrodenitrogenation. [18] However, both $\Delta\Delta H$ and $\Delta\Delta G$ values are larger (less negative) for Co_2P than those over Co(0001) indicating that P does increase the selectivity of Co catalysts toward ^{3}C–O cleavage, but to a lesser extent than it does on Ni. This indicates that the simple presence of P in the catalyst is not enough to shift the selectivity in such a way that the ^{3}C–O activation would be the predominant reaction, but it does make the catalyst more selective towards ^{3}C–O activation in the case of both Ni and Co.

3.5. Selectivity shift for Pd to Pd_2P

The mechanism for C–O activation over Pd(111) and Pd_2P(001) resembles that for Ni(111) and Ni_2P(001), respectively, with one exception. This exception is that ^{2}C–O activation on Pd_2P(001) has a lower relative free energy barrier (307 kJ mol^{-1}) when occurring directly from adsorbed MTHF prior to any dehydrogenation steps (C–O activation barriers of 357 and 329 kJ mol^{-1} after 1 or 2H removals, respectively, Fig. 6c). It is unclear, absent kinetic studies, whether such a change in the mechanism would occur on a Pd_2P surface (one that notably has never been synthesized before). However, this data does add some uncertainty to whether this reaction occurs on Pd_2P via the same mechanism found for Ni_2P(001). MTHF does bind to Pd_2P much the same way as it binds to Ni_2P(001) for both the ^{2}C–O and ^{3}C–O activations (Fig. 5g-h). The same can be seen for Pd(111) in comparison to Ni(111) (Fig. S22).

The $\Delta\Delta G$ values for Pd and Pd_2P show an even greater shift than those for Ni and Ni_2P. These values are calculated using the fully dehydrogenated $\Delta G^{\ddagger}$ for the ^{2}C–O activation (168 and 292 kJ mol^{-1} for Pd and Pd_2P) subtracted by the $\Delta G^{\ddagger}$ for the ^{3}C–O activation (216 and 214 kJ mol^{-1} for Pd and Pd_2P) as described by Equation (17) (Fig. 6). Pd has a more negative $\Delta\Delta G$ value at −86 compared to −74 kJ mol^{-1} for Ni, suggesting it (like Ni) will display high selec-

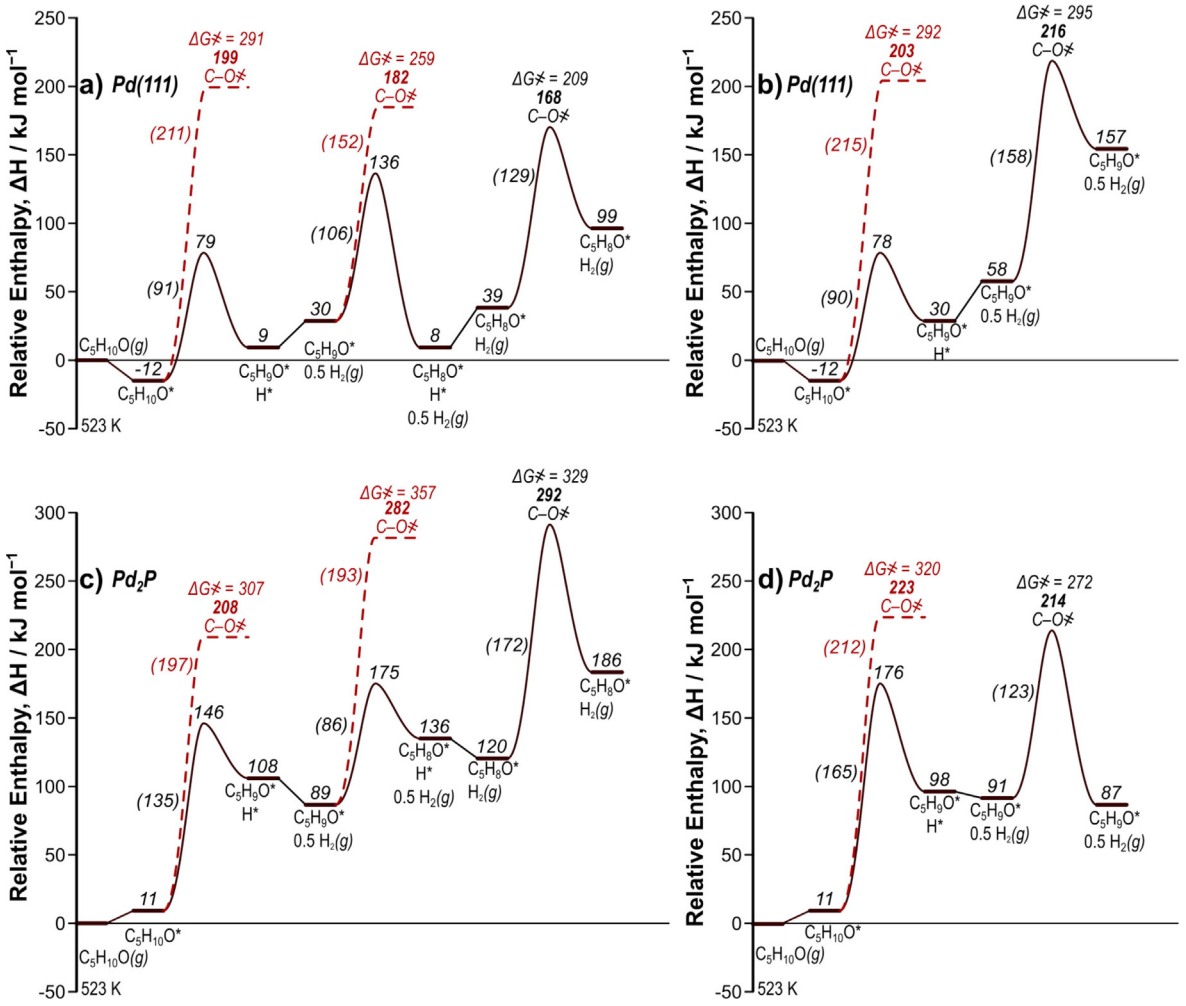

Fig. 6. Reaction coordinate diagrams relative to the bare surface and gas phase MTHF at 523 K for Pd(1 1 1) for the ^{2}C–O bond activation (a) and the ^{3}C–O bond activation (b) along with the reaction coordinate diagrams for Pd_2P(001) for the ^{2}C–O bond activation (c) and the ^{3}C–O bond activation (d). The solid black lines indicate the main (fully dehydrogenated) reaction pathway. The dashed red lines indicate alternate pathways where a C–O bond is activated before full dehydrogenation. The red and black numbers correspond to the relative enthalpies of their respective reactant, product, or transition state. The intrinsic activation barriers (ΔH_{act}) are provided in parentheses for each reaction step. (For interpretation of the references to colour in this figure legend, the reader is referred to the web version of this article.)

tivity towards ^{2}C–O activation. Furthermore, Pd_2P has a much greater $\Delta\Delta G$ value at 57 compared to 0 kJ mol^{-1} for Ni_2P, suggesting that Pd_2P would have excellent selectivity toward ^{3}C–O activation. Overall, this leads to a much greater shift in $\Delta\Delta G$ values in Pd/Pd_2P versus Ni/Ni_2P. Again, this $\Delta\Delta G$ uses the activation free energy for ^{2}C–O cleavage in the fully dehydrogenated intermediate (329 kJ mol^{-1}, Fig. 6c). However, even if one uses the lower value for ^{2}C–O cleavage in intact MTHF (307 kJ mol^{-1}), Pd_2P would still have a $\Delta\Delta G$ value of 35 kJ mol^{-1}, which is still the largest $\Delta\Delta G$ value calculated in our study across all metal-phosphides and pure metal catalysts. Although Pd_2P(001) has not been synthesized, these large shifts in selectivity suggest that other Pd_xP_y (Table 1) are worth exploring for the selective C–O activation of MTHF. Of course, changing the stoichiometry and surface may cause changes in the mechanism and preferred C–O cleavage route, but in our prior work we showed that both Ni_2P and $Ni_{12}P_5$, with distinct stoichiometries and surface structures, led to higher selectivities toward ^{3}C–O bond cleavage than Ni. Also, it may not be entirely surprising that Pd phosphide would show high selectivity for this reaction as other studies have shown PdP_x catalysts to be highly selective for other reactions, specifically involving dehydrogenation.[56,101].

3.6. Selectivity shifts in other transition metals

As shown in our previous work, the $\Delta\Delta G$ between ^{2}C–O and ^{3}C–O activation on Ni-based catalysts increases with P-incorporation, from −74 and −76 on Ni(1 1 1) and (001), respectively, to −13 on $Ni_{12}P_5$ (001) and 0 kJ mol^{-1} on Ni_2P(001), leading toward higher ^{3}C–O activation preferences on NiP_x rather than pure Ni catalysts. These $\Delta\Delta G$ values are shown for Ni and other metal-based catalysts in Fig. 7. For Co, as described in Section 3.4, this shift is much smaller, as the $\Delta\Delta G$ goes from −65 on Co to −54 kJ mol^{-1} on Co_2P. While for Pd, as described in Section 3.5, this shift is very large, as the $\Delta\Delta G$ goes from −86 on Pd to 57 kJ mol^{-1} on Pd_2P. For Fe and Rh, the $\Delta\Delta G$ values were negative (favoring ^{2}C–O cleavage) for both the pure metal and M_2P catalyst surfaces, and as observed for Co, the addition of P to Fe and Rh to make Fe_2P and Rh_2P catalysts cause the $\Delta\Delta G$ values to become less negative, shifting the predicted selectivity in the direction of ^{3}C–O cleavage without making ^{3}C–O cleavage the predominant route. Therefore, for 5 of the 6 metals considered, P shifts the selectivity in the direction of ^{3}C–O cleavage and in two cases (Ni and Pd), it causes ^{3}C–O activation to become the predominant C–O hydrogenolysis pathway. A similar pattern can be seen for ethane dehydrogenation of M_2P sur-

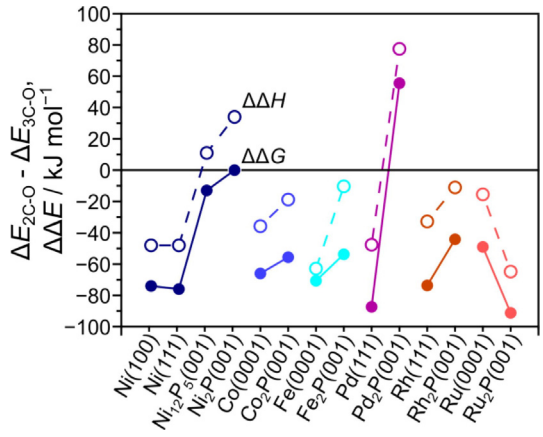

Fig. 7. $\Delta\Delta H$ (open circles and dashed lines) and $\Delta\Delta G$ (solid circles and lines) plots for all of the pure metal and phosphide combinations investigated at 523 K. Data points for these plots were calculated using Equations (17) and (18). Positive values mean a shift in selectivity such that hindered C–O bond activation is favored.

faces where Ni_2P and Pd_2P are significantly more selective toward ethylene desorption than ethylene dehydrogenation in comparison to other M_2P materials (like Fe_2P).[56] However, when comparing Ru_2P ($\Delta\Delta G$ of −90 kJ mol^{-1}) to Ru ($\Delta\Delta G$ of −48 kJ mol^{-1}), there is a decrease in $\Delta\Delta G$ (and $\Delta\Delta H$) values, suggesting that the selectivity shifts further towards activation of the ^{2}C–O bond upon P addition. Ru and Ru_2P thus deviate from the observed shift in selectivity found on all other metals. The aforementioned ethane dehydrogenation study also observed shifts in binding energies of various probe molecules with the addition of P to Ni and other transition metals. These shifts were seen to correlate with the observed shifts in selectivity, however it was not determined why P causes changes in these binding energies.[56,102].

The observed shifts in selectivity are most likely a result of a combination of geometric and electronic effects. Five out of six examined phosphides showed shifts in selectivity towards ^{3}C–O activation, suggesting that there is a nearly ubiquitous shift in selectivity with the addition of P to these metals. However, these shifts do not occur with equal nor with systematic extent. Only two (Ni_2P and Pd_2P) showed a large enough shift such that the tertiary C–O bond activation is the preferred reaction (Fig. 8). This likely means that the structural change that comes about with the addition of P to Ni is not the sole cause for the shift in selectivity towards the hindered C–O activation. If geometric effects were to dominate, we might expect more systematic shifts across all the transition metal phosphides. The varying size of the metal atoms would inherently change the geometry slightly from surface to surface, but the large disparity in the size of the selectivity shifts (and reverse shift with Ru) likely indicate that geometric effects alone do not govern C–O hydrogenolysis in MTHF. Therefore, it follows that the shifts in selectivity of these catalysts results from electronic effects—in part or in whole.

3.7. Periodic trends in C–O activation energies

We observe correlations between the $\Delta\Delta G$ between ^{2}C–O and ^{3}C–O activations and the $\Delta G^{\ddagger}$ barriers through periodic trends in these values. In general, the $\Delta\Delta G$ barriers decrease from Group 8 to Group 10 as well as when moving down from the 3d to the 5d rows for the pure metal surfaces (Fig. 8). However, the $\Delta G^{\ddagger}$ barriers generally increase from Groups 8 to 10 and down the rows. In the case of the M_2P surfaces, $\Delta\Delta G$ and $\Delta G^{\ddagger}$ barriers generally increase from Group 8 to Group 10 as well as when moving down from the 3d to the 5d rows. $\Delta G^{\ddagger}$ barriers are only one piece of information needed to adequately describe the activity of a catalyst. Coverage effects are not within the scope of this investigation. So, in examining these periodic trends, a correlation can only be made between selectivity ($\Delta\Delta G$) and the "nominal" activity ($\Delta G^{\ddagger}$). For the pure metal surfaces, this correlation suggests that moving from Group 8 to Group 10 or moving from row 3d to 5d there is a decrease in both nominal activity and selectivity. The M_2P surfaces show a different correlation with increasing selectivity and decreasing nominal activity moving across the groups and down the rows. As such, Ni_2P and Pd_2P (Group 10) are the most selective materials towards ^{3}C–O activation ($\Delta\Delta G \geq 0$) (Fig. 5), however these phosphides have high activation barriers compared to the other surfaces. On the other hand, Fe_2P and Ru_2P have relatively poor selectivity for ^{3}C–O activation $\Delta\Delta G$ but have the lowest free energy barriers of the metal phosphides. Similar trends were observed for $\Delta H^{\ddagger}$ (Figure S23).

The trends in the $\Delta\Delta G$ values for the pure metal surfaces showed only a weak trend with Group 10 metals (i.e. Ni, Pd, and Pt) being the least selective for ^{3}C–O activation (Fig. 8e). This trend flips and is more pronounced in the phosphide materials, with Ni_2P and Pd_2P (Section 3.1 and 3.3) being the most selective for ^{3}C–O activation. Again, similar trends in $\Delta\Delta H$ (Fig. S24). These trends suggest that the valence shells and other electronic properties of the metals may also play a role in shifting selectivity.

3.8. Origin of the electronic effects

Having established that the increase in selectivity towards ^{3}C–O cleavage is at least partially due to modification of the electronic structure of metal atoms by phosphidation, it now remains to elucidate the exact nature and quantum chemical origin of this electronic effect. Additionally, we seek to understand why this electronic effect is most pronounced on the Group 10 M_2P surfaces while being significantly diminished or reversed on the Group 8 and 9 M_2P surfaces. The simplest explanation would be that phosphorous alters the partial charge on the transition metal atoms, leading to changes in bonding to the C and O atoms in the transition state. To examine this, partial charges were computed on the metal atoms of pure metal and M_2P surfaces using the quasiatomic orbital method (details in Section 2.3). In looking at the average charge of the metal atoms in both the surface layer and the entire surface and both with and without MTHF present, all observed trends were the same. Therefore, the average partial charge over all metal atoms in the top layer of each bare surface (the simplest reference state) is presented in Fig. 9, showing that phosphidation results in a cationic shift in metal atom charge on most M_2P surfaces, the exceptions being Ru_2P and Rh_2P. Electron withdrawal is most pronounced on Ni_2P, with an average removal of 0.3 *e* per surface Ni atom, and decreases upon moving both from right to left along the periodic table and from the 3d to 4d rows (with electron addition occurring on Ru_2P and Rh_2P).

The decrease in electron withdrawal from right to left mirrors the periodic trend of $\Delta\Delta G$, suggesting that the amount of electron withdrawal may be related to the modification of selectivity. This relationship is explored further in Fig. 10, which shows $\Delta\Delta G$ with respect to the average charge on metal atoms in the top layer of each surface. Indeed, a positive correlation is observed between these quantities on all surfaces except Rh/Rh_2P. For example, the metal charge on Pd increases from −0.02 to +0.16 *e*, and the $\Delta\Delta G$ increases from −86 to 57 kJ mol^{-1} upon P incorporation. As described in Section 3.6, Ru_2P is less selective toward ^{3}C–O activation as compared to pure Ru. From this analysis we see that Ru is the only metal that becomes more negatively charged upon P incorporation (−0.02 to −0.08 *e*), suggesting that P incorporation makes it less selective by making Ru more anionic, consistent with the prediction that more-cationic metal atoms have higher ^{3}C–O

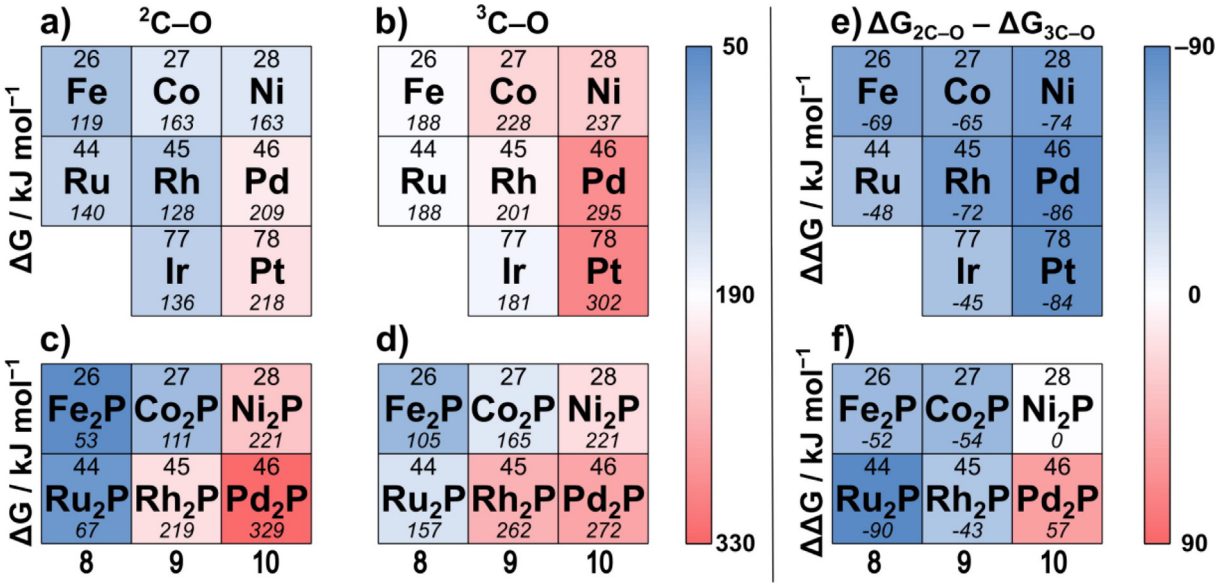

Fig. 8. Periodic table trends for the fully dehydrogenated free energy barriers ($\Delta G^{\ddagger}$, kJ mol^{-1}) for the ^{2}C–O activation for pure metal (a) and M_2P (c) surfaces and ^{3}C–O activation for pure metal (b) and M_2P (d) surfaces. Also, periodic table trends for the difference in fully dehydrogenated free energy barriers ($\Delta\Delta G$, kJ mol^{-1}) relative to the bare surface for the pure metals (e) and the M_2P surfaces (f). Red indicates the most selective towards ^{3}C–O activation and blue indicates the most selective towards ^{2}C–O activation. (For interpretation of the references to colour in this figure legend, the reader is referred to the web version of this article.)

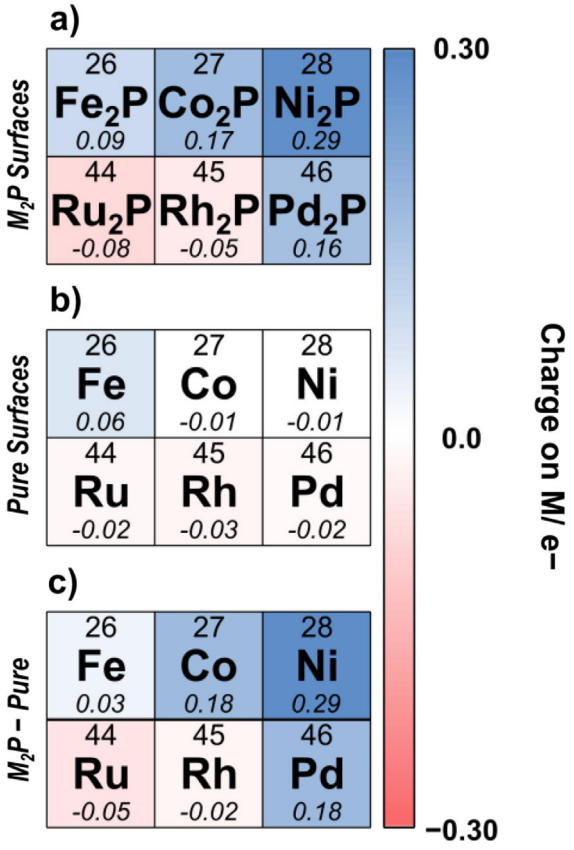

Fig. 9. Periodic trends for the average charge on the metal atoms in the surface layer for both the M_2P (a) and the pure metal (b) surfaces.

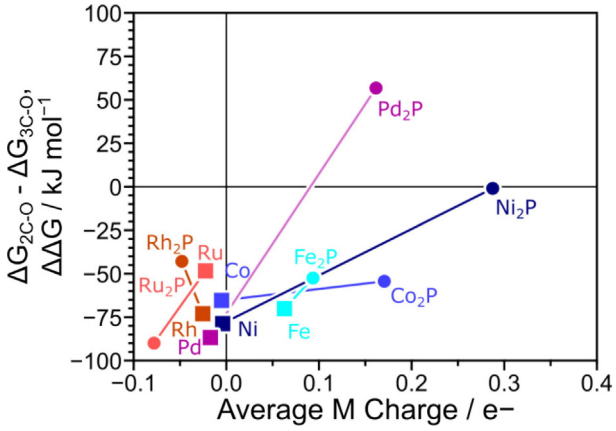

Fig. 10. The difference between the free energies for the ^{2}C–O and ^{3}C–O activations ($\Delta\Delta G$) versus the average charge on the metal atoms in the surface layer for Ni/Ni_2P (navy), Co/Co_2P (blue), Pd/Pd_2P (pink), Fe/Fe_2P (teal), Rh/Rh_2P (orange), and Ru/Ru_2P (coral). (For interpretation of the references to colour in this figure legend, the reader is referred to the web version of this article.)

selectivity. However, the slope of the line for each M/M_2P pair varies significantly with the highest slope observed for Pd/Pd_2P and the weakest (closest to zero) slope for Co. For Rh, the slope is negative, and Rh is the only M/M_2P pair in which the more cationic metal (in pure Rh in this case) is less selective towards ^{3}C–O cleavage than the more anionic metal (in Rh_2P). However, the partial charges calculated within the surfaces of Rh_2P (−0.05 *e*) and pure Rh (−0.03 *e*) are very similar, and it's possible that uncertainties/errors within the partial charge analyses lead to this counter-example more than differences in the underlying physics or chemistry. This discrepancy could also be because factors, other than simple charge effects, likely dominate in causing the observed shift in selectivity. Overall, the varying slopes indicate that while the selectivity modification is likely related to electron withdrawal from the metal by P, there are other effects present that a simple charge analysis cannot uncover.

Assuming that electron withdrawal from the metal by P is the origin of the electronic effect accounting for modification of C–O cleavage selectivity, we additionally desire to identify the quantum chemical origin of the relationship between electron withdrawal and $\Delta\Delta G$. One interpretation of this data is that the electron withdrawal from the metal caused by P is the origin of the enhanced

^{3}C–O selectivity. Under this assumption, the electronegativity of the metal and the M−P ratio would be the primary variables that control selectivity, as those influence the partial charge of the M atoms. Secondary effects, however, may lead to the different slopes shown in Fig. 10, but these effects will likely require further study and more sophisticated probes of the electronic structure such as the constrained orbital DFT.[76] This method allows one to introduce constraints and modifications to the electronic structure in a planewave DFT calculation. In this system of metals and metal phosphides, we envision using the CO-DFT method to perform modifications such as artificially changing the partial charge on metal atoms or disallowing certain types of interactions between the surface and the MTHF (such as π-bonding between M and C or O atoms). We believe a possible explanation for the effect of electronegativity on selectivity is that the transition state for C–O cleavage requires stabilization of the p-orbital on the C as the C–O bond breaks. This occurs by π-bonding with metal d-orbitals. In the ^{2}C–O transition state, the C is bound to two metal atoms, so the C p-orbital has π interactions with both metals. Therefore, each metal formally forms half of a π-bond with the C. In the ^{3}C–O transition state, the C is bound to only one metal atom, so the C p-orbital formally forms a full π-bond with this metal. Withdrawal of electrons from a metal atom removes electrons from the π^* M=C states leading to strengthening of the M=C π-bond. As such, the CO-DFT method[76] may be able to help verify our suspicions on this explanation.

4. Conclusions

The addition of phosphorous to Ni to form $Ni_{12}P_5$(001) and Ni_2P(001) compared to a Ni(111) surface was previously shown to shift the selectivity towards the breaking of the hindered (^{3}C–O) bond in 2-methyltetrahydrofuran (MTHF) with increasing P content. C–O activation was shown to occur by a mechanism where full dehydrogenation of the C atom occurs before C–O activation. Lastly, through kinetic measurements with varying H_2, MTHF, and CO pressures along with DFT-optimized structures, we know that secondary and tertiary C–O activations occur on the same active sites and involve the same number of atoms. DFT calculations show that these sites are comprised of metal ensembles with P not directly taking part in the chemistry.

Here, we investigate whether these selectivity shifts are ubiquitous across a range of transition metals and their associated phosphides. For this study, bulk materials isostructural to Ni_2P (i.e., in the $P\bar{6}2m$ space group) were constructed and optimized for the Pt-group transition metals and in many cases these were theoretical materials that have not been synthesized. Pt_2P, Ir_2P, and Os_2P were excluded from further investigation due to restructuring within their bulk materials. Bulk formation energies further supported the exclusion of these three materials. The remaining bulk structures were cleaved to form M_2P(001) surfaces for which surface formation energies were calculated, justifying further study of these surfaces. The thermodynamic and activation enthalpies and free energies were calculated for each step of the secondary and tertiary C–O activation pathways on these surfaces and corresponding close-packed pure metal surfaces.

For all of the pure metal and phosphide surfaces, the predicted mechanism is consistent with the one presented for Ni(111) and Ni_2P(001) in previous work. All C–H activations have a lower enthalpic barrier than the corresponding C–O activation for that step. Also, except for the ^{2}C–O activation on Pd_2P, the C–O activation after full dehydrogenation has the lowest $\Delta G^{\neq}$ barrier for each surface and pathway. To predict selectivities between ^{2}C–O and ^{3}C–O activations, $\Delta\Delta H$ and $\Delta\Delta G$ values were calculated for each pure metal and metal phosphide combination. Pd_2P(001) in comparison to Pd(111) showed a similar trend in selectivity to Ni ($\Delta\Delta G$ of 57 and −86 kJ mol^{-1} respectively), suggesting that PdP_x materials should be tested experimentally for this reaction. Co_2P, Fe_2P, and Rh_2P showed slight shifts toward ^{3}C–O bond activation in comparison to their pure metal counterparts. However, these surfaces still showed a preference for the ^{2}C–O bond activation. Lastly, Ru_2P(001) showed an opposite shift, away from ^{3}C–O activation, in comparison to Ru(0001). Because five of the six transition metal phosphides investigated do show shifts in selectivity toward hindered bond activation, there is some evidence that geometric effects play a role in the selectivity shift, but it does not appear to be a dominant factor, given the variable selectivity shifts (strongly toward ^{3}C–O in Pd and Ni, weakly toward ^{3}C–O in Co, Fe, and Rh, and toward ^{2}C–O for Ru). Therefore, a combination of geometric and electronic effects is likely what drives the shift in selectivity seen with the addition of P to Ni.

Periodic trends were observed both for free energy barriers of fully dehydrogenated C–O activations and for $\Delta\Delta G$ values. For the free energy barriers, across both C–O activations and across both pure metal and phosphide surfaces a similar trend of increasing $\Delta G^{\neq}$ values going right along the periodic table is seen. For the $\Delta\Delta G$ values, there is a flip in trends when shifting from the pure metals to the metal phosphides. The metal surfaces indicate a weak trend of increasing selectivity for the ^{2}C–O activation going right across the periodic table. Meanwhile, the phosphide surfaces indicate increasing selectivity for the ^{3}C–O activation moving right across the periodic table. Together these trends indicate that the most selective surfaces for the hindered C–O activation also have the highest activation barriers to overcome possibly indicating an inverse relationship between activity and selectivity. However, activation barriers do not adequately predict activity. Ni and Pd phosphides were the only two surfaces to show a preference for hindered C–O bond activation. Because these two metals are in the same periodic group, this suggests some form of electronic effects influence the shift in selectivity. This analysis shows that for five of the six M/M_2P combinations in this study, the surface with the more cationic metal adsorption site has the higher selectivity suggesting that in general more cationic adsorption sites lead to high selectivity. The lone exception, Rh, has very similar partial charges in both the pure Rh and Rh_2P surfaces, and thus secondary factors unrelated to charge transfer may have larger effects for those surfaces. Therefore, more sophisticated tools are needed to fully elucidate the electronic effects of adding P to transition metal catalysts. Other methods that may be useful include investigating other materials that may be isostructural to Ni_2P(001) such as M_2As, M_2Si, and M_2N structures to further understand geometric and electronic effects. Other materials such as oxides could prove useful for understanding more on electron withdrawal between metal and nonmetal atoms, but oxides tend to lack metal ensemble sites which make them poor candidates for this type of study. Furthermore, in this manuscript, we use theoretical materials that are isostructural to Ni_2P(001) and found that Pd_2P shows the greatest selectivity for ^{3}C–O activation. In Section 3.2 we also list a variety of PdP_x materials that have been experimentally synthesized. Prior work on NiP_x materials shows that both $Ni_{12}P_5$ and Ni_2P showed enhanced ^{3}C–O selectivity compared to Ni, thus indicating that the synthesized PdP_x materials, although structurally distinct from the Pd_2P examined here, are worthwhile catalyst candidates for these materials.

Data availability

Data will be made available on request.

Declaration of Competing Interest

The authors declare the following financial interests/personal relationships which may be considered as potential competing interests: David Hibbitts reports financial support was provided by National Science Foundation.

Acknowledgements

This work was funded by the National Science Foundation [NSF-#CHE-1954426]. Computational resources were provided by the Advanced Cyberinfrastructure Coordination Ecosystem: Services & Support (ACCESS) and University of Florida Research Computing.

Appendix A. Supplementary data

Supplementary data to this article can be found online at https://doi.org/10.1016/j.jcat.2023.02.011.

References

[1] D. Carpenter, T.L. Westover, S. Czernik, W. Jablonski, Biomass feedstocks for renewable fuel production: a review of the impacts of feedstock and pretreatment on the yield and product distribution of fast pyrolysis bio-oils and vapors, Green Chem. 16 (2014) 384–406, https://doi.org/10.1039/C3GC41631C.

[2] D. Mohan, C.U. Pittman, P.H. Steele, Pyrolysis of Wood/Biomass for Bio-oil: A Critical Review, Energy Fuels. 20 (2006) 848–889, https://doi.org/10.1021/ef0502397.

[3] A. Oasmaa, S. Czernik, Fuel oil quality of biomass pyrolysis oilsstate of the art for the end users, Energy Fuels. 13 (1999) 914–921, https://doi.org/10.1021/ef980272b.

[4] Y. Zeng, S. Zhao, S. Yang, S.-Y. Ding, Lignin plays a negative role in the biochemical process for producing lignocellulosic biofuels, Curr. Opin. Biotechnol. 27 (2014) 38–45, https://doi.org/10.1016/j.copbio.2013.09.008.

[5] M. Saidi, F. Samimi, D. Karimipourfard, T. Nimmanwudipong, B.C. Gates, M.R. Rahimpour, Upgrading of lignin-derived bio-oils by catalytic hydrodeoxygenation, Energy Environ. Sci. 7 (2014) 103–129, https://doi.org/10.1039/C3EE43081B.

[6] E.A. Roldugina, E.R. Naranov, A.L. Maximov, E.A. Karakhanov, Hydrodeoxygenation of guaiacol as a model compound of bio-oil in methanol over mesoporous noble metal catalysts, Appl. Catal. A 553 (2018) 24–35, https://doi.org/10.1016/j.apcata.2018.01.008.

[7] H.Y. Zhao, D. Li, P. Bui, S.T. Oyama, Hydrodeoxygenation of guaiacol as model compound for pyrolysis oil on transition metal phosphide hydroprocessing catalysts, Appl. Catal. A 391 (2011) 305–310, https://doi.org/10.1016/j.apcata.2010.07.039.

[8] E. Furimsky, Catalytic hydrodeoxygenation, Appl. Catal. A 199 (2000) 147–190, https://doi.org/10.1016/S0926-860X(99)00555-4.

[9] M. Chia, Y.J. Pagán-Torres, D. Hibbitts, Q. Tan, H.N. Pham, A.K. Datye, M. Neurock, R.J. Davis, J.A. Dumesic, Selective hydrogenolysis of polyols and cyclic ethers over bifunctional surface sites on rhodium-rhenium catalysts, J. Am. Chem. Soc. 133 (2011) 12675–12689, https://doi.org/10.1021/ja2038358.

[10] Top Value Added Chemicals from Biomass - Volume II, Results of Screening for Potential Candidates from Biorefinery Lignin (Program Document) | OSTI. GOV, (n.d.). https://www.osti.gov/biblio/1216434 (accessed March 8, 2022).

[11] D.M. Alonso, J.Q. Bond, J.A. Dumesic, Catalytic conversion of biomass to biofuels, Green Chem. 12 (2010) 1493, https://doi.org/10.1039/c004654j.

[12] P.P. Bui, S.T. Oyama, A. Takagaki, B.P. Carrow, K. Nozaki, Reactions of 2-Methyltetrahydropyran on Silica-Supported Nickel Phosphide in Comparison with 2-Methyltetrahydrofuran, ACS Catal. 6 (2016) 4549–4558, https://doi.org/10.1021/acscatal.6b01033.

[13] A. Cho, H. Kim, A. Iino, A. Takagaki, S. Ted Oyama, Kinetic and FTIR studies of 2-methyltetrahydrofuran hydrodeoxygenation on Ni 2 P/SiO 2, J. Catal. 318 (2014) 151–161, https://doi.org/10.1016/j.jcat.2014.07.021.

[14] A. Cho, A. Takagaki, R. Kikuchi, S. Ted Oyama, Active Sites in Ni_2P/USY Catalysts for the Hydrodeoxygenation of 2-Methyltetrahydrofuran, Top. Catal. 58 (2015) 219–231, https://doi.org/10.1007/s11244-015-0363-3.

[15] A. Iino, A. Cho, A. Takagaki, R. Kikuchi, S. Ted Oyama, Kinetic studies of hydrodeoxygenation of 2-methyltetrahydrofuran on a Ni2P/SiO2 catalyst at medium pressure, J. Catal. 311 (2014) 17–27, https://doi.org/10.1016/j.jcat.2013.11.002.

[16] M.E. Witzke, A. Almithn, C.L. Coonrod, D.D. Hibbitts, D.W. Flaherty, Mechanisms and Active Sites for C-O Bond Rupture within 2-Methyltetrahydrofuran over Ni, Ni_{12} P_5, and Ni_2 P Catalysts, ACS Catal. 8 (2018) 7141–7157, https://doi.org/10.1021/acscatal.7b04403.

[17] R. Prins, M.E. Bussell, Metal phosphides: preparation, characterization and catalytic reactivity, Catal. Lett. 142 (2012) 1413–1436, https://doi.org/10.1007/s10562-012-0929-7.

[18] S.T. Oyama, Novel catalysts for advanced hydroprocessing: transition metal phosphides, J. Catal. 216 (2003) 343–352, https://doi.org/10.1016/S0021-9517(02)00069-6.

[19] I.I. Abu, K.J. Smith, HDN and HDS of model compounds and light gas oil derived from Athabasca bitumen using supported metal phosphide catalysts, Appl. Catal. A 328 (2007) 58–67, https://doi.org/10.1016/j.apcata.2007.05.018.

[20] C.V.M. Inocêncio, P.M. de Souza, R.C. Rabelo-Neto, V.T. da Silva, F.B. Noronha, A systematic study of the synthesis of transition metal phosphides and their activity for hydrodeoxygenation of phenol, Catal. Today. 381 (2021) 133–142, https://doi.org/10.1016/j.cattod.2020.07.077.

[21] R.H. Bowker, M.C. Smith, M.L. Pease, K.M. Slenkamp, L. Kovarik, M.E. Bussell, Synthesis and hydrodeoxygenation properties of ruthenium phosphide catalysts, ACS Catal. 1 (2011) 917–922, https://doi.org/10.1021/cs200238v.

[22] P. Bui, J.A. Cecilia, S. Ted, A. Oyama, A. Takagaki, H. Infantes-Molina, D. Zhao, E. Li, A.J. Rodríguez-Castellón, López,, Studies of the synthesis of transition metal phosphides and their activity in the hydrodeoxygenation of a biofuel model compound, J. Catal. 294 (2012) 184–198, https://doi.org/10.1016/j.jcat.2012.07.021.

[23] S.T. Oyama, T. Gott, H. Zhao, Y.-K. Lee, Transition metal phosphide hydroprocessing catalysts: A review, Catal. Today. 143 (2009) 94–107, https://doi.org/10.1016/j.cattod.2008.09.019.

[24] P. Liu, J.A. Rodriguez, Catalytic properties of molybdenum carbide, nitride and phosphide: A theoretical study, Catal. Lett. 91 (2003) 247–252, https://doi.org/10.1023/B:CATL.0000007163.01772.19.

[25] A. Almithn, Z. Alhulaybi, A mechanistic study of methanol steam reforming on ni2p catalyst, Catalysts 12 (2022) 1174, https://doi.org/10.3390/catal12101174.

[26] R.B. Wexler, J.M.P. Martirez, A.M. Rappe, Chemical Pressure-Driven Enhancement of the Hydrogen Evolving Activity of Ni2P from Nonmetal Surface Doping Interpreted via Machine Learning, J. Am. Chem. Soc. 140 (2018) 4678–4683, https://doi.org/10.1021/jacs.8b00947.

[27] M. Peroni, G. Mancino, E. Baráth, O.Y. Gutiérrez, J.A. Lercher, Bulk and γ–Al_2O_3-supported Ni_2P and MoP for hydrodeoxygenation of palmitic acid, Appl. Catal. B. 180 (2016) 301–311, https://doi.org/10.1016/j.apcatb.2015.06.042.

[28] J.A. Cecilia, A. Infantes-Molina, E. Rodríguez-Castellón, A. Jiménez-López, S.T. Oyama, Oxygen-removal of dibenzofuran as a model compound in biomass derived bio-oil on nickel phosphide catalysts: Role of phosphorus, Appl. Catal. B. 136–137 (2013) 140–149, https://doi.org/10.1016/j.apcatb.2013.01.047.

[29] S.-K. Wu, P.-C. Lai, Y.-C. Lin, Atmospheric Hydrodeoxygenation of Guaiacol over Nickel Phosphide Catalysts: Effect of Phosphorus Composition, Catal. Lett. 144 (2014) 878–889, https://doi.org/10.1007/s10562-014-1231-7.

[30] K. Li, R. Wang, J. Chen, Hydrodeoxygenation of Anisole over Silica-Supported Ni_2P, MoP, and NiMoP Catalysts, Energy Fuels. 25 (2011) 854–863, https://doi.org/10.1021/ef101258j.

[31] A. Cho, J. Shin, A. Takagaki, R. Kikuchi, S.T. Oyama, Ligand and Ensemble Effects in Bimetallic NiFe Phosphide Catalysts for the Hydrodeoxygenation of 2-Methyltetrahydrofuran, Top. Catal. 55 (2012) 969–980, https://doi.org/10.1007/s11244-012-9882-3.

[32] J. Chen, Y. Yang, H. Shi, M. Li, Y. Chu, Z. Pan, X. Yu, Regulating product distribution in deoxygenation of methyl laurate on silica-supported Ni–Mo phosphides: Effect of Ni/Mo ratio, Fuel 129 (2014) 1–10, https://doi.org/10.1016/j.fuel.2014.03.049.

[33] Highly selective bimetallic FeMoP catalyst for C-O bond cleavage of aryl ethers | Health & Environmental Research Online (HERO) | US EPA, (n.d.). https://hero.epa.gov/hero/index.cfm/reference/details/reference_id/2893963 (accessed March 9, 2022).

[34] S. Ted Oyama, T. Onkawa, A. Takagaki, R. Kikuchi, S. Hosokai, Y. Suzuki, K.K. Bando, Production of Phenol and Cresol from Guaiacol on Nickel Phosphide Catalysts Supported on Acidic Supports, Top. Catal. 58 (2015) 201–210, https://doi.org/10.1007/s11244-015-0361-5.

[35] H. Shi, J. Chen, Y. Yang, S. Tian, Catalytic deoxygenation of methyl laurate as a model compound to hydrocarbons on nickel phosphide catalysts: Remarkable support effect, Fuel Process. Technol. 118 (2014) 161–170, https://doi.org/10.1016/j.fuproc.2013.08.010.

[36] S.-K. Wu, P.-C. Lai, Y.-C. Lin, H.-P. Wan, H.-T. Lee, Y.-H. Chang, Atmospheric Hydrodeoxygenation of Guaiacol over Alumina-, Zirconia-, and Silica-Supported Nickel Phosphide Catalysts, ACS Sustain. Chem. Eng. 1 (2013) 349–358, https://doi.org/10.1021/sc300157d.

[37] J.-S. Moon, E.-G. Kim, Y.-K. Lee, Active sites of Ni2P/SiO2 catalyst for hydrodeoxygenation of guaiacol: A joint XAFS and DFT study, J. Catal. 311 (2014) 144–152, https://doi.org/10.1016/j.jcat.2013.11.023.

[38] A.S. Almithn, D.D. Hibbitts, Impact of metal and heteroatom identities in the hydrogenolysis of C-X bonds (X = C, N, O, S, and cl), ACS Catal. 10 (2020) 5086–5100, https://doi.org/10.1021/acscatal.0c00481.

[39] J. Feng, B. Xu, Reaction Mechanisms for the Heterogeneous Hydrogenolysis of Biomass-Derived Glycerol to Propanediols, Prog. Rct. Kin. Mech. 39 (2014) 1–15, https://doi.org/10.3184/97809059274714X13874723178485.

[40] K. Tomishige, Y. Nakagawa, M. Tamura, Selective hydrogenolysis of C-O bonds using the interaction of the catalyst surface and OH groups, Top. Curr. Chem. 353 (2014) 127–162, https://doi.org/10.1007/128_2014_538.

[41] D.W. Flaherty, D.D. Hibbitts, E. Iglesia, Metal-catalyzed C-C bond cleavage in alkanes: effects of methyl substitution on transition-state structures and stability, J. Am. Chem. Soc. 136 (2014) 9664–9676, https://doi.org/10.1021/ja5037429.

[42] D.W. Flaherty, E. Iglesia, Transition-state enthalpy and entropy effects on reactivity and selectivity in hydrogenolysis of n-alkanes, J. Am. Chem. Soc. 135 (2013) 18586–18599, https://doi.org/10.1021/ja4093743.
[43] D.D. Hibbitts, D.W. Flaherty, E. Iglesia, Effects of chain length on the mechanism and rates of metal-catalyzed hydrogenolysis of n-alkanes, J. Phys. Chem. C. 120 (2016) 8125–8138, https://doi.org/10.1021/acs.jpcc.6b00323.
[44] D.D. Hibbitts, D.W. Flaherty, E. Iglesia, Role of branching on the rate and mechanism of C-C cleavage in alkanes on metal surfaces, ACS Catal. 6 (2016) 469–482, https://doi.org/10.1021/acscatal.5b01950.
[45] D.W. Flaherty, D.D. Hibbitts, E.I. Gürbüz, E. Iglesia, Theoretical and kinetic assessment of the mechanism of ethane hydrogenolysis on metal surfaces saturated with chemisorbed hydrogen, J. Catal. 311 (2014) 350–356, https://doi.org/10.1016/j.jcat.2013.11.026.
[46] G.C. Bond, J.C. Slaa, Catalytic and structural properties of ruthenium bimetallic catalysts: hydrogenolysis of propane and n-butane on RuAl2O3 catalysts modified by a Group 14 element, J. Mol. Catal. A: Chem. 106 (1996) 135–149, https://doi.org/10.1016/1381-1169(95)00245-6.
[47] R.T. Hannagan, G. Giannakakis, R. Réocreux, J. Schumann, J. Finzel, Y. Wang, A. Michaelides, P. Deshlahra, P. Christopher, M. Flytzani-Stephanopoulos, M. Stamatakis, E.C.H. Sykes, First-principles design of a single-atom–alloy propane dehydrogenation catalyst, Science 372 (2021) 1444–1447, https://doi.org/10.1126/science.abg8389.
[48] R.D. Cortright, J.A. Dumesic, Microcalorimetric, spectroscopic, and kinetic studies of silica supported pt and pt/sn catalysts for isobutane dehydrogenation, J. Catal. 148 (1994) 771–778, https://doi.org/10.1006/jcat.1994.1263.
[49] J. Llorca, N. Homs, J. León, J. Sales, J.L.G. Fierro, P. Ramirez de la Piscina, Supported Pt–Sn catalysts highly selective for isobutane dehydrogenation: preparation, characterization and catalytic behavior, Appl. Catal. A 189 (1999) 77–86, https://doi.org/10.1016/S0926-860X(99)00253-7.
[50] B. Coq, F. Fgiueras, Geometric and electronic effects in the conversion of methylcyclopentane on Pt-Sn catalysts, J. Mol. Catal. 25 (1984) 87–98, https://doi.org/10.1016/0304-5102(84)80033-4.
[51] A. Dasgupta, E.K. Zimmerer, R.J. Meyer, R.M. Rioux, Generalized approach for the synthesis of silica supported Pd-Zn, Cu-Zn and Ni-Zn gamma brass phase nanoparticles, Catal. Today. (2018), https://doi.org/10.1016/j.cattod.2018.10.050.
[52] H. Zhou, X. Yang, L. Li, X. Liu, Y. Huang, X. Pan, A. Wang, J. Li, T. Zhang, PdZn Intermetallic Nanostructure with Pd–Zn–Pd Ensembles for Highly Active and Chemoselective Semi-Hydrogenation of Acetylene, ACS Catal. 6 (2016) 1054–1061, https://doi.org/10.1021/acscatal.5b01933.
[53] F. Studt, F. Abild-Pedersen, T. Bligaard, R.Z. Sørensen, C.H. Christensen, J.K. Nørskov, Identification of non-precious metal alloy catalysts for selective hydrogenation of acetylene, Science 320 (2008) 1320–1322, https://doi.org/10.1126/science.1156660.
[54] J. Osswald, R. Giedigkeit, R. Jentoft, M. Armbruster, F. Girgsdies, K. Kovnir, T. Ressler, Y. Grin, R. Schlogl, Palladium–gallium intermetallic compounds for the selective hydrogenation of acetylenePart I: Preparation and structural investigation under reaction conditions, J. Catal. 258 (2008) 210–218, https://doi.org/10.1016/j.jcat.2008.06.013.
[55] R.J. Meyer, Q. Zhang, A. Kryczka, C. Gomez, R. Todorovic, Perturbation of Reactivity with Geometry: How Far Can We Go?, ACS Catal 8 (2018) 566–570, https://doi.org/10.1021/acscatal.7b03228.
[56] J. Ko, W.F. Schneider, Computational screen of M_2 P metal phosphides for catalytic ethane dehydrogenation, Catal, Sci. Technol. 12 (2022) 5629–5639, https://doi.org/10.1039/D2CY00602B.
[57] G. Kresse, J. Furthmüller, Efficiency of ab-initio total energy calculations for metals and semiconductors using a plane-wave basis set, Comp. Mater. Sci. 6 (1996) 15–50, https://doi.org/10.1016/0927-0256(96)00008-0.
[58] G. Kresse, J. Furthmüller, Efficient iterative schemes for *ab initio* total-energy calculations using a plane-wave basis set, Phys. Rev. B. 54 (1996) 11169–11186, https://doi.org/10.1103/PhysRevB.54.11169.
[59] G. Kresse, J. Hafner, Ab initio molecular dynamics for open-shell transition metals, Phys Rev, B Condens Matter. 48 (1993) 13115–13118, https://doi.org/10.1103/physrevb.48.13115.
[60] G. Kresse, J. Hafner, Ab initio molecular-dynamics simulation of the liquid-metal-amorphous-semiconductor transition in germanium, Phys. Rev. B. 49 (1994) 14251–14269, https://doi.org/10.1103/PhysRevB.49.14251.
[61] P. Kravchenko, C. Plaisance, D. Hibbitts, A new computational interface for catalysis, Published as pre-print on https://chemrxiv.org/articles/preprint/8040737 (2019). https://doi.org/10.26434/chemrxiv.8040737.v3.
[62] G. Kresse, D. Joubert, From ultrasoft pseudopotentials to the projector augmented-wave method, Phys. Rev. B. 59 (1999) 1758–1775, https://doi.org/10.1103/PhysRevB.59.1758.
[63] P.E. Blöchl, Projector augmented-wave method, Phys. Rev. B. 50 (1994) 17953–17979, https://doi.org/10.1103/PhysRevB.50.17953.
[64] B. Hammer, L.B. Hansen, J.K. Nørskov, Improved adsorption energetics within density-functional theory using revised Perdew-Burke-Ernzerhof functionals, Phys. Rev. B. 59 (1999) 7413–7421, https://doi.org/10.1103/PhysRevB.59.7413.
[65] J.P. Perdew, K. Burke, M. Ernzerhof, Generalized gradient approximation made simple, Phys. Rev. Lett. 77 (1996) 3865–3868, https://doi.org/10.1103/PhysRevLett.77.3865.
[66] Y. Zhang, W. Yang, Comment on "Generalized Gradient Approximation Made Simple," Phys. Rev. Lett. 80 (1998) 890–890. https://doi.org/10.1103/PhysRevLett.80.890.
[67] J. Ren, J. Wang, J. Li, Y. Li, Density functional theory study on crystal nickel phosphides, J. Fuel Chem. Technol. 35 (2007) 458–464, https://doi.org/10.1016/S1872-5813(07)60029-2.
[68] A. Taylor, Lattice parameters of binary nickel cobalt alloys, J. Inst. Met. 77 (1950) 585–594.
[69] E. Larsson, An X-ray investigation of Ni-P system and crystal structures of NiP and NiP2, Arkiv Kemi. 23 (1965).
[70] S. Rundqvist, M. Yhland, R. Dahlbom, J. Sjövall, O. Theander, H. Flood, X-Ray Investigations of Mn3P, Mn2P, and Ni2P, Acta Chem. Scand. 16 (1962) 992–998, https://doi.org/10.3891/acta.chem.scand.16-0992.
[71] M.G. Moula, S. Suzuki, W.-J. Chun, S. Otani, S.T. Oyama, K. Asakura, The First Atomic-scale Observation of a Ni_2P(0001) Single Crystal Surface, Chem. Lett. 35 (2006) 90–91, https://doi.org/10.1246/cl.2006.90.
[72] G. Henkelman, H. Jónsson, Improved tangent estimate in the nudged elastic band method for finding minimum energy paths and saddle points, J. Chem. Phys. 113 (2000) 9978–9985, https://doi.org/10.1063/1.1323224.
[73] H. Jónsson, G. Mills, K.W. Jacobsen, Nudged elastic band method for finding minimum energy paths of transitions, in: B.J. Berne, G. Ciccotti, D.F. Coker (Eds.), Classical and Quantum Dynamics in Condensed Phase Simulations, World Scientific, 1998, pp. 385–404, https://doi.org/10.1142/9789812839664_0016.
[74] G. Henkelman, H. Jónsson, A dimer method for finding saddle points on high dimensional potential surfaces using only first derivatives, J. Chem. Phys. 111 (1999) 7010–7022, https://doi.org/10.1063/1.480097.
[75] X. Qian, J. Li, L. Qi, C.-Z. Wang, T.-L. Chan, Y.-X. Yao, K.-M. Ho, S. Yip, Quasiatomic orbitals for *ab initio* tight-binding analysis, Phys. Rev. B. 78 (2008), https://doi.org/10.1103/PhysRevB.78.245112.
[76] C.P. Plaisance, R.A. van Santen, K. Reuter, Constrained-Orbital Density Functional Theory. Computational Method and Applications to Surface Chemical Processes, J. Chem. Theory Comput. 13 (2017) 3561–3574, https://doi.org/10.1021/acs.jctc.7b00362.
[77] A. Jain, S.P. Ong, G. Hautier, W. Chen, W.D. Richards, S. Dacek, S. Cholia, D. Gunter, D. Skinner, G. Ceder, K.A. Persson, Commentary: The Materials Project: A materials genome approach to accelerating materials innovation, APL Mater. 1 (2013), https://doi.org/10.1063/1.4812323.
[78] S. Gražulis, D. Chateigner, R.T. Downs, A.F.T. Yokochi, M. Quirós, L. Lutterotti, E. Manakova, J. Butkus, P. Moeck, A. Le Bail, Crystallography Open Database - an open-access collection of crystal structures, J. Appl. Crystallogr. 42 (2009) 726–729, https://doi.org/10.1107/S0021889809016690.
[79] A. Vaitkus, A. Merkys, S. Gražulis, Validation of the Crystallography Open Database using the Crystallographic Information Framework, J. Appl. Crystallogr. 54 (2021) 661–672, https://doi.org/10.1107/S1600576720016532.
[80] M. Quirós, S. Gražulis, S. Girdzijauskaitė, A. Merkys, A. Vaitkus, Using SMILES strings for the description of chemical connectivity in the Crystallography Open Database, J. Cheminform. 10 (2018) 23, https://doi.org/10.1186/s13321-018-0279-6.
[81] S. Gražulis, A. Daškevič, A. Merkys, D. Chateigner, L. Lutterotti, M. Quirós, N.R. Serebryanaya, P. Moeck, R.T. Downs, A. Le Bail, Crystallography Open Database (COD): an open-access collection of crystal structures and platform for world-wide collaboration, Nucleic Acids Res. 40 (2012) D420–D427, https://doi.org/10.1093/nar/gkr900.
[82] A. Merkys, A. Vaitkus, J. Butkus, M. Okulič-Kazarinas, V. Kairys, S. Gražulis, *COD::CIF::Parser*: an error-correcting CIF parser for the Perl language, J. Appl. Crystallogr. 49 (2016) 292–301, https://doi.org/10.1107/S1600576715022396.
[83] S. Gražulis, A. Merkys, A. Vaitkus, M. Okulič-Kazarinas, Computing stoichiometric molecular composition from crystal structures, J. Appl. Crystallogr. 48 (2015) 85–91, https://doi.org/10.1107/S1600576714025904.
[84] S. Furuseth, K. Selte, A. Kjekshus, P.H. Nielsen, B. Sjöberg, E. Larsen, Redetermined Crystal Structures of PdAs2, PdSb2, PtP2, PtAs2, PtSb2, alpha-PtBi2, and AuSb2, Acta Chem. Scand. 19 (1965) 735–741, https://doi.org/10.3891/acta.chem.scand.19-0735.
[85] A. Kjekshus, T. Rakke, A.F. Andresen, J.O. Thomas, Compounds with the Marcasite Type Crystal Structure. XII. Structural Data for RuP2, RuAs2, RuSb2, OsP2, OsAs2, and OsSb2., Acta Chem. Scand. 31a (1977) 253–259. https://doi.org/10.3891/acta.chem.scand.31a-0253.
[86] S. Rundqvist, A. Hede, S. Rundqvist, E. Varde, G. Westin, X-Ray Investigation on Rhodium Phosphides. The Crystal Structure of Rh4P3, Acta Chem. Scand. 14 (1960) 893–902, https://doi.org/10.3891/acta.chem.scand.14-0893.
[87] W. Wong-Ng, W.Y. Ching, Y.-N. Xu, J.A. Kaduk, I. Shirotani, L. Swartzendruber, Structure and electronic properties of the orthorhombic MoRuP superconductor prepared at high pressure, Phys. Rev. B. 67 (2003), https://doi.org/10.1103/PhysRevB.67.144523.
[88] T. MatkoviĆ, K. Schubert, Kristallstruktur von Pd7P3, J. the Less Common Metals 55 (1977) 177–184, https://doi.org/10.1016/0022-5088(77)90190-4.
[89] B. Lv, B.I. Jawdat, Z. Wu, M. Sorolla, M. Gooch, K. Zhao, L. Deng, Y.-Y. Xue, B. Lorenz, A.M. Guloy, C.-W. Chu, Synthesis, structure, and superconductivity in the new-structure-type compound: SrPt6P2, Inorg. Chem. 54 (2015) 1049–1054, https://doi.org/10.1021/ic502377v.
[90] B. Carlsson, M. Gölin, S. Rundqvist, Determination of the homogeneity range and refinement of the crystal structure of Fe2P, J. Solid State Chem. 8 (1973) 57–67, https://doi.org/10.1016/0022-4596(73)90021-2.

[91] G.L. Viali, G.R. Gonçalves, E.C. Passamani, J.C.C. Freitas, M.A. Schettino, A.Y. Takeuchi, C. Larica, Magnetic and hyperfine properties of Fe 2 P nanoparticles dispersed in a porous carbon matrix, J. Magn. Magn. Mater. 401 (2016) 173–179, https://doi.org/10.1016/j.jmmm.2015.10.028.
[92] N. Available, Materials Data on Fe2P by Materials Project, LBNL Materials Project; Lawrence Berkeley National Laboratory (LBNL), Berkeley, CA (United States). (2020), https://doi.org/10.17188/1305394.
[93] X. Chen, M. Cheng, D. Chen, R. Wang, Shape-Controlled Synthesis of Co2P Nanostructures and Their Application in Supercapacitors, ACS Appl. Mater. Interfaces. 8 (2016) 3892–3900, https://doi.org/10.1021/acsami.5b10785.
[94] J.F. Callejas, C.G. Read, E.J. Popczun, J.M. McEnaney, R.E. Schaak, Nanostructured Co_2 P Electrocatalyst for the Hydrogen Evolution Reaction and Direct Comparison with Morphologically Equivalent CoP, Chem. Mater. 27 (2015) 3769–3774, https://doi.org/10.1021/acs.chemmater.5b01284.
[95] N. Available, Materials Data on Co2P by Materials Project, LBNL Materials Project; Lawrence Berkeley National Laboratory (LBNL), Berkeley, CA (United States). (2020), https://doi.org/10.17188/1197421.
[96] K. Persson, Materials Data on Co2P (SG:189) by Materials Project, LBNL Materials Project; Lawrence Berkeley National Laboratory (LBNL), Berkeley, CA (United States). (2014), https://doi.org/10.17188/1189589.
[97] H. Zhang, D.-H. Ha, R. Hovden, L.F. Kourkoutis, R.D. Robinson, Controlled synthesis of uniform cobalt phosphide hyperbranched nanocrystals using tri-n-octylphosphine oxide as a phosphorus source, Nano Lett. 11 (2011) 188–197, https://doi.org/10.1021/nl103400a.
[98] N. Available, Materials Data on PRu2 by Materials Project, LBNL Materials Project; Lawrence Berkeley National Laboratory (LBNL), Berkeley, CA (United States). (2020), https://doi.org/10.17188/1197248.
[99] N. Available, Materials Data on PRh2 by Materials Project, LBNL Materials Project; Lawrence Berkeley National Laboratory (LBNL), Berkeley, CA (United States). (2020), https://doi.org/10.17188/1201530.
[100] N. Available, Materials Data on PIr2 by Materials Project, LBNL Materials Project; Lawrence Berkeley National Laboratory (LBNL), Berkeley, CA (United States). (2017), https://doi.org/10.17188/1196023.
[101] A. Sampath, D.W. Flaherty, Effects of phosphorus addition on selectivity and stability of Pd model catalysts during cyclohexene dehydrogenation, Catal, Sci. Technol. 10 (2020) 993–1005, https://doi.org/10.1039/C9CY02134E.
[102] J. Ko, H. Ma, W.F. Schneider, Kinetic origins of high selectivity of metal phosphides for ethane dehydrogenation, Ind. Eng. Chem. Res. (2022), https://doi.org/10.1021/acs.iecr.2c02044.